Time-Domain Analysis of a Phase-Shift-Modulated Series Resonant Converter with an Adaptive Passive Auxiliary Circuit

Alireza Safaee, *Senior Member, IEEE*, Masoud Karimi-Ghartemani, *Senior Member, IEEE*, Praveen K. Jain, *Fellow, IEEE*, and Alireza Bakhshai, *Senior Member, IEEE*

***Abstract*—This paper presents a comprehensive time-domain analysis of series resonant converters operating with phase-shift-modulated full-bridge above resonance. Closed-form formulas for all quantities are derived using two methods: the commonly used fundamental harmonic approximation as well as a precise time-domain analysis considering the effect of all the harmonics. Detailed analytical method describes steady-state behavior of the converter in three mutually exclusive and collectively exhaustive modes of operation based on continuity of the resonant inductor current: a discontinuous mode and two continuous modes. The difference between two continuous modes is in the existence of natural zero-voltage switching in the leading leg of the full bridge. Quantitative predictions of the key quantities from two methods are compared and the accuracy of the first harmonic approximation is examined. The time-domain approach provides useful insights for design considerations with no need to know the load value. It precisely determines closed-form equations for the boundary conditions of the three operation modes. An adaptive passive auxiliary circuit is suggested to guarantee zero-voltage switching for the entire operating conditions. Experimental results from a 100 W prototype confirm the predicted time-domain behavior and achievement of soft switching using the proposed auxiliary circuit.**

***Index Terms*—Adaptive auxiliary circuit, continuous current mode (CCM), dc–dc converter, discontinuous current mode (DCM), full bridge, passive auxiliary circuit, series resonant converter (SRC), time-domain analysis, zero-voltage switching (ZVS).**

I. Introduction

DC/DC series resonant converters (SRCs) have been introduced decades ago as high-efficiency power converter topologies [1]. Recently, the trend toward miniaturization of power converters (especially in transportation) and availability of wide band-gap devices have revived the attention to resonant converters [2]–[10]. In addition, the emerging technology of wireless power transfer applies the resonant converter concepts extensively [11]–[16]. The advantages of the SRC are: intrinsic low switching losses (which allows operating at higher switching frequencies), taking advantage of inevitable parasitic inductances as a part of resonant tank, lower electromagnetic interference (EMI) levels, higher power density, a single capacitor as output filer, flat efficiency versus load, and intrinsic short circuit protection due to having the resonant inductance in series with the load.

An output-voltage-regulated SRC works on the basis of voltage split between a lossless impedance (the resonant tank) and an energy-absorbing equivalent ac resistance (which resembles the dc load) in a way that the voltage across the latter remains constant. Study of square wave frequency-controlled SRC in frequency domain is provided in [17] for continuous current mode (CCM) and more completely in [18]–[20]. State-plane diagram is another common analysis method [21]–[24]. Time-domain analysis is a powerful analysis method and is utilized in [25]–[32] and with a loosely coupled transformer in [33]. The dynamic behavior of the square wave SRC is analyzed in the time domain as well in [34]–[36]. In a SRC with variable frequency control technique, a wide range of operating frequencies is needed to achieve output voltage regulation against variations in input voltage or load level (and still at no-load conditions the output voltage regulation is not achievable). This wide frequency variation brings disadvantages such as severe constraints on the gate drivers, difficult EMI filter design due to the wide frequency spectrum, and nonlinearities due to variable ratio of deadtime/switching period.

For the aforementioned disadvantages of variable frequency control, a fixed-frequency control method is favored. Driving the resonant tank by a full-bridge structure allows for several modulation schemes other than frequency modulation [37], [38]. For pulse width and phase-shift modulations, the existence of two operation modes based on the continuity of the resonant tank current is reported in [39]. Results in [39] are for operating at the exact resonant frequency, obtained by a time-domain analysis. Boundary conditions are also specified in [39] which are valid solely for operating at the resonant frequency. Having two distinct CCMs for above resonant operation is shown in [40] without a time-domain analysis or a criterion for the mode boundary conditions. In [41]–[43], three modes are distinguished without closed-form equations for the mode boundaries. The presence of two kinds of boundaries between discontinuous current mode

Manuscript received December 28, 2015; revised March 15, 2016; accepted April 7, 2016. Date of publication April 21, 2016; date of current version June 24, 2016. Recommended for publication by M. Ponce-Silva.

A. Safaee was with the ePOWER, Department of Electrical and Computer Engineering, Queens University, Kingston, ON K7L 3N6 Canada. He is now with OSRAM Sylvania, Beverly, MA 01915 USA (e-mail: az_safaee@ieee.org).

M. Karimi-Ghartemani is with the Department of Electrical and Computer Engineering, Mississippi State University, Starkville, MS 39762 USA (e-mail: karimi@ece.msstate.edu).

P. K. Jain and A. Bakhshai are with the ePOWER, Department of Electrical and Computer Engineering, Queens University, Kingston, ON K7L 3N6 Canada (e-mail: praveen.jain@queensu.ca).

This paper has supplementary downloadable multimedia material available at http://ieeexplore.ieee.org provided by the authors. The material is 0.2 MB in size.

Color versions of one or more of the figures in this paper are available online at http://ieeexplore.ieee.org.

Digital Object Identifier 10.1109/TPEL.2016.2557725

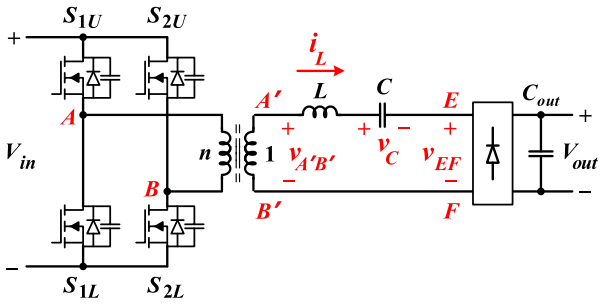

Fig. 1. SRC with full-bridge inverter and full-bridge diode rectifier.

(DCM) and continuous modes are reported in [44] using time-domain analysis without differentiating between two continuous modes. The boundary conditions in this reference are provided as functions of the output power level above which converter will enter to the continuous mode. This method of representing boundary conditions is difficult to use in practice.

In this paper, the time-domain method of Safaee *et al.* [45] is extended and the following aspects are addressed: exact closed-form equations for all the circuit parameters in three operational modes are extracted for all possible values of voltage ratio and phase shift. Analytical formulas for the power, mode boundaries, and triple point are derived. Also, equations for the point with the highest power and the point with the largest leading leg current during transition are obtained. None of these equations require the quality factor which is a load-dependent parameter.

This paper is organized as follows: in Section II, the general SRC with phase-shift modulation and wide output range is introduced and the assumptions are clarified. In Section III, analysis of SRC in steady state using fundamental harmonic approximation (FHA) is provided and three operation modes, their boundary conditions, and main equations are derived. Section IV provides the detailed time-domain analysis of all main quantities for the three modes of operation. Section V includes exact equations for the boundary conditions and triple points. Section VI includes an objective comparison between the predictions of the same converter under FHA and with time-domain methods. Section VII provides the experimental results confirming the analytical predictions and Section VIII discusses the effect of nonzero drain–source capacitance and deadtime.

II. SRC

An SRC circuit using a full-bridge inverter is depicted in Fig. 1. The input voltage $V_{\rm in}$ passes through the EMI filter and feeds the dc bus of the inverter (EMI filter and the dc bus capacitor are not shown in Fig. 1). The switch leg labeled by A (B) on its ac node is composed of switches S_{1L} and S_{1U} (S_{2L} and S_{2U}) and is referred to as the leading (lagging) leg throughout this paper. The transformer is connected between the ac nodes of the inverter and has a primary-secondary turns ratio of $n:1$. The resonant tank includes an inductor L and a capacitor C, and is the interface between the transformer and the rectifier diode bridge. The rectified current is filtered by a dc capacitor $C_{\rm out}$, to generate the output voltage $V_{\rm out}$.

The common approach in study of SRC is as follows. The analysis starts by assuming that the values of these quantities are known: $V_{\rm in}$, L, C, n, $f_{\rm SW}$ (inverter switching frequency), R_L (load resistance), and φ (the phase-shift angle, in the case of a phase-shift modulated full-bridge inverter in SRC). Then, calculation is done to have $V_{\rm out}$, P (power), $I_{L\_\max}$ (resonant tank peak current), $I_{L\rm rms}$ (resonant tank effective current), $V_{C\_\max}$ (resonant capacitor peak voltage) and more. $I_{L\_\max}$ and $V_{C\_\max}$ are needed to select the components with sufficient margins. $I_{L\rm rms}$ is required to evaluate the conduction losses for thermal design. This approach needs approximations to have an analytic prediction of $V_{\rm out}$. The FHA is widely used here, which is based on the second-order bandpass filter behavior of the series connection of the resonant inductor and capacitor. Due to operating close to the resonant frequency (to have a low overall voltage drop across the tank), FHA assumes that the current in the tank has a sinusoidal waveform. An equivalent ac resistor $R_{\rm eq}$ is introduced to calculate the voltage split between the lossless impedance of the resonant tank at the switching frequency, Z, and $R_{\rm eq}$. Then, the voltage across $R_{\rm eq}$ is obtained which can determine $V_{\rm out}$.

The achieved formula for $V_{\rm out}$ is an approximated one and its accuracy should be justified. Although it is possible to consider the higher harmonics, the equations will be in the sigma format and getting insights from them is not straightforward. Also, the predicted $V_{\rm out}$ depends directly on R_L, often hidden in another parameter named as the quality factor. In practice, R_L is not a part of the converter and its information is not available to the controller; therefore, the formula for $V_{\rm out}$ as function of R_L is not directly applicable for controller design.

The approach in this paper meets the following requirements:

1) exact analysis of SRC considering the effect of all the harmonics in a set of closed-form equations;
2) prediction of P, $I_{L\_\max}$, I_{Lrms}, $V_{C\_\max}$ and zero-voltage switching (ZVS) condition of the converter analytically only based on the values known to the controller, with no need to know load resistance or quality factor;
3) precise determination of three distinct modes of operation and closed form formulas for the boundary conditions;
4) objective assessment of the precision of FHA predictions.

The following assumptions are considered for the analysis:

1) all passive components in the circuit are ideal with no equivalent series resistance, the load resistance ensures reaching the steady-state operation;
2) the transformer is linear, lossless, and its magnetizing current is negligible, the leakage inductance of the transformer is absorbed in the resonant inductance;
3) the converter switching frequency is constant and greater than the resonant frequency;
4) the converter uses the phase-shift modulation scheme and has settled in steady-state operation;
5) output capacitor is large and output voltage is constant with no ripple. The variation range of $V_{\rm out}$ is from zero to $V_{\rm in}$.

Assumption 1 is based on the fact that in an SRC with a high efficiency (>90%) all the components in the current path from the source to the load should be designed with minimum

series resistances. This is true for the input capacitor, switches, transformer, resonant tank elements, rectifier diodes, output capacitor and printed circuit board. The newer generations of semiconductor devices and capacitors have significantly reduced series resistances. If any of the elements has a large resistance sufficient to impact the governing time-domain equations of the converter, it will also severely reduce the total converter efficiency. Therefore, as we are studying the voltage gain and soft switching of properly designed SRCs, it can be assumed that the series resistances are negligible.

Assumption 2 tells us that the transformers in SRCs are usually designed to have minimum losses and this requires selecting the maximum flux density of the magnetic core in the linear region of the *B–H* curve. Also, for a proper transformer with a tight coupling between primary and secondary windings, the magnetizing inductance is often at least two orders of magnitude larger than the leakage inductances. Thus, as far as the voltage gain and soft-switching aspects are concerned, the magnetizing current can be safely neglected.

In practice, the specifications of an output-voltage-regulated dc–dc converter usually guarantee less than 1% for the maximum peak-to-peak voltage ripple at the output terminal. In an SRC, the output capacitor provides the low impedance path for the ac component of the rectified current after the diode bridge. This requires the output capacitor to have a low equivalent resistance and reactance at double the switching frequency. Therefore, in steady state, we can ignore the variations in $V_{\rm out}$. This is the rationale of Assumption 5.

III. Analysis of SRC in Steady State Using FHA

In this paper, an approach is selected which is slightly different than (and fully equivalent to) the aforementioned one. The rationale is as follows: in steady-state operation, the converter has settled down at the desired level of $V_{\rm out}$ known to the controller via feedback. Also, $V_{\rm in}$ is sampled and known by the controller. The approach here is to start from the known $V_{\rm in}$ and $V_{\rm out}$ (instead of $V_{\rm in}$ and R_L) and calculate the main quantities. First, the essential parameters of the converter are defined

$$\omega_0 = \frac{1}{\sqrt{LC}}\,, \quad Z_0 = \sqrt{L/C}\,, \quad \omega_{\rm SW} = \frac{2\pi}{T}$$
$$M = \frac{V_{\rm out}}{V_{\rm in}/n}\,, \quad r = \frac{\omega_{\rm SW}}{\omega_0} \tag{1}$$

where ω_0, Z_0, $\omega_{\rm SW}$, T, M, n, and r are the angular resonant frequency, characteristic impedance, angular switching frequency, switching period, dc voltage ratio, primary-to-secondary turns ratio of the transformer, and frequency ratio, respectively.

A. CCMs

Typical voltage and current waveforms of SRC operation using FHA are shown in Fig. 2. Symbol φ is the phase shift between the ac voltages of the leading leg, v_A, and that of lagging leg, v_B, in radians, which is controlled by the control unit. Also $\theta_{\rm FHA}$ in Fig. 2 is the phase angle between the symmetry axes

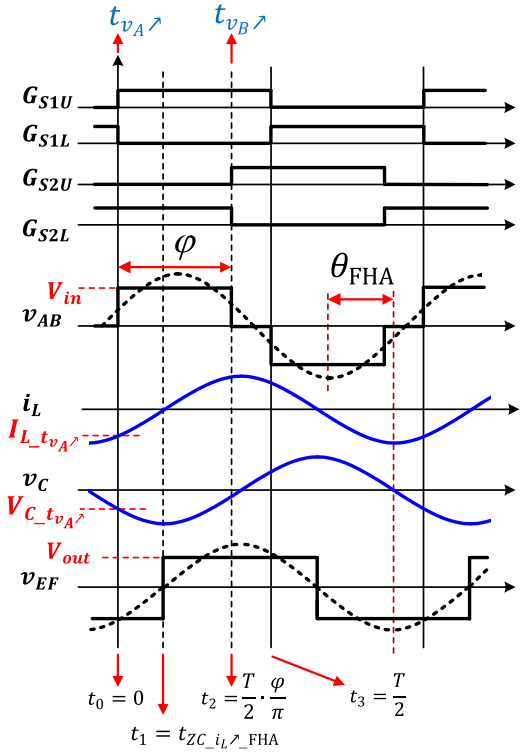

Fig. 2. Major voltage and current waveforms of SRC using FHA.

of v_{AB} and $v_{\rm EF}$. Hereafter, all quantities with subscript FHA indicate the fundamental harmonic approximation. The dashed lines in Fig. 2 depict the fundamental harmonics of v_{AB} and $v_{\rm EF}$ denoted by $v_{AB\_\rm FHA}$ and $v_{\rm EF\_FHA}$.

Due to the large magnetization inductance of the transformer, there is only one possibility for the resonant current to flow, i.e., through the rectifier bridge. Therefore, the SRC is operational only if the condition $V_{\rm in} \geq nV_{\rm out}$ or equivalently $M \leq 1$ is satisfied (neglecting an anomalous operation reported in [46]). There is no dc component in i_L (a pure sinusoidal waveform). Note that $v_{\rm EF}$ is in phase with i_L due to the existence of the rectifier bridge and therefore $v_{\rm EF}$ has a 50% duty-cycle.

Another aspect of having the sinusoidal resonant current i_L under FHA is that the transferred power from AB side to EF side depends only on the first harmonics of $v_{A'B'} = v_{AB}/n$ and $v_{\rm EF}$, denoted by $v_{A'B'\_\rm FHA}$ and $v_{\rm EF\_FHA}$, and their higher order harmonics do not contribute in the transferred power. Therefore, it is possible to continue the study using the phasors of $v_{A'B'\_\rm FHA}$ and $v_{\rm EF\_FHA}$ in the calculations, $\vec{V}_{A'B'\text{-}\rm FHA}$ and $\vec{V}_{\rm EF\_FHA}$, respectively. The amplitudes of the phasors are

$$\left|\vec{V}_{A'B'\_\rm FHA}\right| = \frac{4}{\pi}V\cdot\frac{V_{\rm in}}{n}\sin\frac{\varphi}{2}$$
$$\left|\vec{V}_{\rm EF\_FHA}\right| = \frac{4}{\pi}V_{\rm out} = \frac{4}{\pi}\cdot\frac{V_{\rm in}}{n}M. \tag{2}$$

Fig. 3 shows the phasor diagram of $\vec{V}_{A'B'\text{-}\rm FHA}$, $\vec{V}_{\rm EF\_FHA}$, and $\vec{I}_{L\_\rm FHA}$. The angles are compatible with the selection of the rising moment of v_A as $t = 0$ in Fig. 2. Due to the rectifier bridge, the phasors $\vec{V}_{\rm EF\_FHA}$ and $\vec{I}_{L\_\rm FHA}$ are always parallel.

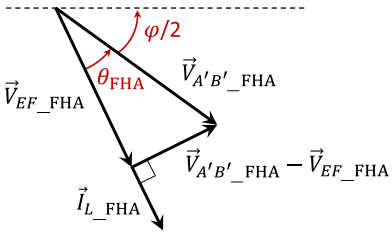

Fig. 3. Phasor diagram of major voltages and resonant current under FHA.

From Fig. 3, the angle $\theta_{\rm FHA}$ can be calculated as follows:

$$\cos\theta_{\rm FHA} = \frac{\left|\vec{V}_{\rm EF\_FHA}\right|}{\left|\vec{V}_{A'B'\_FHA}\right|} = \frac{M}{\sin\frac{\varphi}{2}}. \tag{3}$$

Equation (3) determines the range of validity of the FHA. For a continuous current to exist the ratio of $M/\sin\frac{\varphi}{2}$ must satisfy $0 \le M \le \sin\frac{\varphi}{2}$. Having this condition in place, the amplitude of the resonant current phasor can be calculated from Fig. 3

$$\begin{aligned}\left|\vec{I}_{L\_FHA}\right| &= \frac{\left|\vec{V}_{A'B'\_FHA}\right|\sin\theta_{\rm FHA}}{Z} = \frac{4}{\pi Z}\cdot\frac{V_{\rm in}}{n}\sin\frac{\varphi}{2}\ \sin\theta_{\rm FHA} \\ &= \frac{4}{\pi Z}\cdot\frac{V_{\rm in}}{n}\sqrt{\sin^2\frac{\varphi}{2}-M^2}\end{aligned} \tag{4}$$

where the value of the impedance Z is

$$Z = L\omega_{\rm SW} - \frac{1}{(C\omega_{\rm SW})} = Z_0\left(r - \frac{1}{r}\right). \tag{5}$$

Therefore

$$\left|\vec{I}_{L\_FHA}\right| = I_{\rm base}\times\frac{4r}{\pi^2\left(r^2-1\right)}\cdot\sqrt{\sin^2\frac{\varphi}{2}-M^2} \tag{6}$$

with $I_{\rm base}$ defined in and used throughout this paper

$$I_{\rm base} \triangleq \frac{\pi}{Z_0}\left(\frac{V_{\rm in}}{n}\right). \tag{7}$$

Also, the active power is

$$\begin{aligned}P_{\rm FHA} &= \frac{1}{2Z}\left|\vec{V}_{A'B'\_FHA}\right|\left|\vec{V}_{\rm EF\_FHA}\right|\sin\theta_{\rm FHA} \\ &= \frac{8M}{\pi^2 Z}\cdot\left(\frac{V_{\rm in}}{n}\right)^2\sin\frac{\varphi}{2}\ \sin\theta_{\rm FHA} \\ &= \frac{8}{\pi^2 Z}\left(\frac{V_{\rm in}}{n}\right)^2 M\sqrt{\sin^2\frac{\varphi}{2}-M^2}\end{aligned} \tag{8}$$

which can be represented as

$$P_{\rm FHA} = P_{\rm base}\times\frac{4rM}{\pi^2\left(r^2-1\right)}\sqrt{\sin^2\frac{\varphi}{2}-M^2} \tag{9}$$

with $P_{\rm base}$ defined in (10) and used hereafter

$$P_{\rm base} \triangleq \frac{2}{Z_0}\left(\frac{V_{\rm in}}{n}\right)^2. \tag{10}$$

The ac equivalent resistance and the dc load resistance which absorb the power P_{H1} are

$$R_{\rm eq\_FHA} = \frac{P_{\rm FHA}}{\left|\vec{I}_{L\_FHA}\right|^2/2} = \frac{MZ}{\sqrt{\sin^2\frac{\varphi}{2}-M^2}} \tag{11}$$

$$\begin{aligned}R_{\rm Load\_FHA} &= \frac{V_{\rm out}^2}{P_{\rm FHA}} = \frac{\left(MV_{\rm in}/n\right)^2}{\frac{8M}{\pi^2 Z}\left(\frac{V_{\rm in}}{n}\right)^2\sqrt{\sin^2\frac{\varphi}{2}-M^2}} \\ &= \frac{\pi^2 MZ}{8\sqrt{\sin^2\frac{\varphi}{2}-M^2}} = \frac{\pi^2}{8}R_{\rm eq\_FHA}\end{aligned} \tag{12}$$

which is compatible with the standard frequency-domain analysis of SRCs.

The zero-crossing moment of i_{L_FHA} when it goes from negative to positive (negative to positive) values, denoted by $t_{\rm ZC\_i_L\nearrow\_FHA}$ ($t_{\rm ZC\_i_L\searrow\_FHA}$), is found as

$$\begin{aligned}t_{\rm ZC\_i_L\nearrow\_FHA} &= \frac{1}{\omega_{\rm SW}}\left(\frac{\varphi}{2}+\theta_{\rm FHA}-\frac{\pi}{2}\right) \\ t_{\rm ZC\_i_L\searrow\_FHA} &= t_{\rm ZC\_i_L\nearrow FHA}+\frac{T}{2}.\end{aligned} \tag{13}$$

And the $I_{L\_t_{v_A}\nearrow\_FHA}$ in Fig. 2 is

$$I_{L\_t_{v_A}\nearrow\_FHA} = \left|\vec{I}_{L\_FHA}\right|\cos\left(\frac{\varphi}{2}+\theta_{\rm FHA}\right). \tag{14}$$

The maximum voltage of the resonant capacitor is

$$V_{C\_max\_FHA} = \frac{4}{\pi\left(r^2-1\right)}\sqrt{\sin^2\frac{\varphi}{2}-M^2}\cdot\left(\frac{V_{\rm in}}{n}\right). \tag{15}$$

So far, it clear that the selected approach describes the entire behavior of the converter. To show that this approach is equivalent to the common approach in predicting the voltage gain (i.e., M) as a function of $V_{\rm in}$ and R_L, we use the definition of quality factor as

$$Q = \frac{\sqrt{L/C}}{\frac{8}{\pi^2}R_L} = \frac{\pi^2}{8}\times\frac{Z_0}{R_L}. \tag{16}$$

Power is governed by

$$P = \frac{\left(V_{\rm out}\right)^2}{R_L} = \frac{4}{\pi^2}M^2Q\times P_{\rm base}. \tag{17}$$

By substituting $P_{\rm base}$ from (9) in (17), M can be calculated as

$$M_{\rm FHA} = \frac{\sin\frac{\varphi}{2}}{\sqrt{Q^2(r-1/r)^2+1}} \tag{18}$$

which is a well-known equation for SRC under FHA.

B. DCM

Equation (3) reveals that the converter operates in DCM when the condition $\sin\frac{\varphi}{2} \le M \le 1$ holds. Because the basis of the FHA is on assuming a sinusoidal waveform for the resonant current, which is continuous versus time by definition, no predictions for DCM can be expected from FHA.

C. Mode Boundaries

The boundary condition of DCM and CCM modes can be found from (3). The specific φ where the condition $M = \sin\frac{\varphi}{2}$ holds is denoted by $\varphi_{\mathrm{DCM\_CCM\_FHA}}$ and is given by

$$\varphi_{\mathrm{DC\_CCM\_FHA}}\ (M) = 2\sin^{-1}M. \tag{19}$$

Substituting $M = \sin(\varphi_{\mathrm{DCM\_CCM\_FHA}}/2)$ in (3) leads to $\theta_{\mathrm{FHA}} = 0$. At this condition, $|\vec{V}_{A'B'\_\mathrm{FHA}}| - |\vec{V}_{\mathrm{EF})\_\mathrm{FHA}}| = 0$ which means that $\vec{I}_{L\_\mathrm{FHA}}$ is identical to zero. The immediate consequence is

$$P_{\mathrm{DCM\_CCM\_FHA}}\ (M) = 0. \tag{20}$$

CCM can be further split to two distinct modes based on the sign of $I_{L\_t_{v_A}\nearrow\_\mathrm{FHA}}$ in (14). The mode with $I_{L\_t_{v_A}\nearrow\_\mathrm{FHA}} > 0$ is called CCM1 and the mode with $I_{L\_t_{v_A}\nearrow\_\mathrm{FHA}} < 0$ is named as CCM2. The boundary between CCM1 and CCM2 can be found from $t_{\mathrm{ZC\_i_L}\nearrow\_\mathrm{FHA}} = 0$ (due to the selection of the rising edge of v_A as $t = 0$ in Fig. 2). The value of φ at this point is named as $\varphi_{\mathrm{CCM1\_CCM2\_FHA}}$ and is given by

$$\varphi_{\mathrm{CCM1\_CCM2\_FHA}}\ (M) = 2\sin^{-1}\sqrt{M}. \tag{21}$$

Substituting $\varphi_{\mathrm{CCM1\_CCM2\_FHA}}$ in (8) results in

$$P_{\mathrm{CCM1\_CCM2\_FHA}}(M) = P_{\mathrm{base}} \times \frac{4rM\sqrt{M(1-M)}}{\pi^2(r^2-1)} \tag{22}$$

$$\left|\vec{I}_{L\_\mathrm{CCM1\_CCM2\_FHA}}\right| = \frac{4}{\pi Z}\cdot\frac{V_{\mathrm{in}}}{n}\sqrt{M(1-M)} = I_{\mathrm{base}} \times \frac{4r\sqrt{M(1-M)}}{\pi^2(r^2-1)}. \tag{23}$$

1) Continuous Current Mode 1 (CCM1): In this mode $I_{L\_t_{v_A}\nearrow\_\mathrm{FHA}}$ has positive values. This means that the leading leg does not have natural ZVS operation in this mode. In other words, the transition from turning off of S_{1L} and turning on of S_{1U} does not happen with ZVS which requires $I_{L\_t_{v_A}\nearrow\_\mathrm{FHA}}$ to be sufficiently negative (to provide energy to change/discharge the drain–source capacitors of the switches). Having $I_{L\_t_{v_A}\nearrow\_\mathrm{FHA}} > 0$ means that the negative-to-positive zero-crossing moment of i_L happens before the rising edge of v_A, or $t_{\mathrm{ZC\_i_L}\nearrow\_\mathrm{FHA}} < 0$. The condition to be in CCM1 mode is

$$2\sin^{-1}M = \varphi_{\mathrm{DCM\_CCM\_FHA}}(M) \le \varphi(M) \le \varphi_{\mathrm{CCM1\_CCM2\_FHA}}(M) = 2\sin^{-1}\sqrt{M}. \tag{24}$$

Equations (4)–(14) are valid for this mode of operation.

As the values of $I_{L\_t_{v_A}\nearrow\_\mathrm{FHA}}$ in this mode are positive, it is possible to find the specific operating point where the maximum $I_{L\_t_{v_A}\nearrow\_\mathrm{FHA}}$ occurs. The importance of this maximum current point is discussed in following sections for designing an auxiliary circuit to ensure ZVS. By substituting θ_{FHA} from (3) in (4) $|\vec{I}_{L\_\mathrm{FHA}}|$ is found and then from (14) $I_{L\_t_{v_A}\nearrow\_\mathrm{FHA}}$ is determined. The maximum $I_{L\_t_{v_A}\nearrow\_\mathrm{FHA}}$ happens at

$$\varphi_{I_{L\_t_{v_A}\nearrow\_\mathrm{max\_FHA}}} = \frac{\pi}{3} \quad \text{and} \quad M_{I_{L\_t_{v_A}\nearrow\_\mathrm{max\_FHA}}} = \frac{\sqrt{3}}{4}. \tag{25}$$

Note that under FHA the location of this maximum point does not depend on r. The maximum $I_{L\_t_{v_A}\nearrow\_\mathrm{FHA}}$ is

$$I_{L\_t_{v_A}\nearrow\_\mathrm{max\_FHA}} = \frac{1}{2\pi Z}\cdot\frac{V_{\mathrm{in}}}{n} = I_{\mathrm{base}} \times \frac{r}{2\pi^2(r^2-1)}. \tag{26}$$

The $I_{L\_t_{v_A}\nearrow\_\mathrm{max\_FHA}}$ value does vary by r through the dependence of Z on r given in (5).

2) Continuous Current Mode 2 (CCM2): In this mode, $I_{L\_t_{v_A}\nearrow\_\mathrm{FHA}}$ is negative and the leading leg operates under ZVS because $I_{L\_t_{v_A}\nearrow\_\mathrm{FHA}}$ provides the energy needed for changing/discharging the drain–source capacitors of the switches. Having $I_{Lt_{v_A}\nearrow\_\mathrm{FHA}} < 0$ means that the negative-to-positive zero-crossing moment of i_L happens after the rising edge of v_A or $t_{\mathrm{ZCi_L}\nearrow\mathrm{FHA}} > 0$. The condition to be in CCM2 mode is

$$2\sin^{-1}\sqrt{M} = \varphi_{\mathrm{CCM1CCM2FHA}}\ (M) \le \varphi(M) \le \pi. \tag{27}$$

All (4)–(14) are again valid for this mode of operation.

The maximum power point occurs in CCM2. From (8) it is clear that P_{FHA} increases at higher φ numbers; therefore, the maximum power happens at $\varphi = \pi$. Maximum power form (8) is

$$M_{P_{\mathrm{max\_FHA}}} = \frac{1}{\sqrt{2}} \quad \text{and} \quad P_{\mathrm{max\_FHA}} = \frac{4}{\pi^2 Z}\left(\frac{V_{\mathrm{in}}}{n}\right)^2 = P_{\mathrm{base}} \times \frac{2r}{\pi^2(r^2-1)}. \tag{28}$$

Similar to the case of the maximum current point in (25), the location of the maximum power point does not change by r. Equation (28) also reveals that dependence of $P_{\mathrm{max\_FHA}}$ on r is only through variation of Z with r as given in (5). From (12) and (16) with (28), we find

$$R_{L\_P_{\mathrm{max\_FHA}}} = \frac{\pi^2}{8} \times \frac{(r^2-1)}{r} Z_0 \tag{29}$$

$$Q_{P_{\mathrm{max\_FHA}}} = \frac{r}{r^2-1}. \tag{30}$$

$R_{L\_P_{\mathrm{max\_FHA}}}$ and $Q_{P_{\mathrm{max\_FHA}}}$ represent the load resistance and quality factor at the maximum power point under FHA. Equations (12) and (29) give

$$R_{L\_P_{\mathrm{max\_FHA}}} = \frac{\pi^2}{8} \times Z. \tag{31}$$

Also from (5) and (31)

$$R_{\mathrm{eq\_}P_{\mathrm{max\_FHA}}} = Z \tag{32}$$

which is expected because for a voltage split between ac resistors Z and R_{eqFHA} the power delivered to latter is maximum when the condition in (32) holds.

Following the representations in [23], the boundaries are visualized in Fig. 4 which is a plane of operating points with $0 \le M \le 1$ and $0^\circ \le \varphi \le 180^\circ$ on the horizontal and vertical axes, respectively. The lower boundary belongs to DCM–CCM1 border and is predicted by (19). The upper boundary is the CCM1–CCM2 boundary and is governed by (21). Based

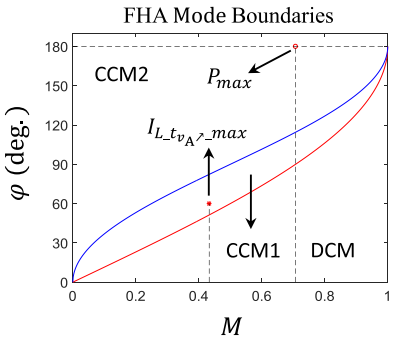

Fig. 4 Mode boundaries predicted by FHA. Points of $I_{L\_t_{v_A\nearrow}\_\max}$ in CCM1 and $P_{\max}$ in CCM2 are shown.

on FHA, mode CCM1 separates DCM and CCM2 regions for all M values. The maximum $I_{Lt_{v_A\nearrow}\_\mathrm{FHA}}$ point in CCM1, from (25), and the maximum power point in CCM2, from (28), are also shown in Fig. 4. The boundaries and maximum points are independent of r, based on FHA. These predictions are in accordance with [23] and [24]. The readers are encouraged to refer to the accompanied "SRC_Modes" calculator described in the Appendix.

This section revealed that FHA correctly predicts three distinct modes with analytical predictions for the phasors of the voltages and the resonant tank current, the soft-switching conditions, and the power. FHA however cannot describe the converter behavior in DCM which requires a more precise analysis. Such precise method can also determine the validity range of the FHA predictions. The next section provides the time-domain analysis of the SRC.

IV. Analysis of SRC in Steady State Using Exact Time-Domain Approach

In this section, the time-domain approach is used to analyze the behavior of SRC under phase-shift modulation for the widest output voltage range and to complete the previous studies in [45]. The selected approach is to solve the time-domain state equations and to find functions for the state variables $i_L(t)$ and $v_C(t)$ using the properties such as piecewise continuity and half-cycle antisymmetry (resulted from the steady-state operation).

A. DCM

There are three intervals in each half-cycle of SRC operating at DCM and the equivalent circuits for them are depicted in Fig. 5. Typical voltage and current waveforms are shown in Fig. 6. The other half-cycle is known from the half-cycle antisymmetry

1) Interval 1: $0 \le t \le \frac{T}{2} \times \frac{\varphi}{\pi}$*:* The switching cycle starts with interval 1 at the rising (falling) edge of $G_{S1U}(G_{S1L})$. At $t_0 = 0$, the inductor current I_{Lt0} is zero due to the discontinuous nature of the inductor current in this mode, and thus $t_{\mathrm{ZCi_L}\nearrow} = 0$. The resonant capacitor has the voltage of V_{Ct_0} to be determined. $v_{A'B'}$ is equal to V_{in}/n and v_{EF} is equal to V_{out}.

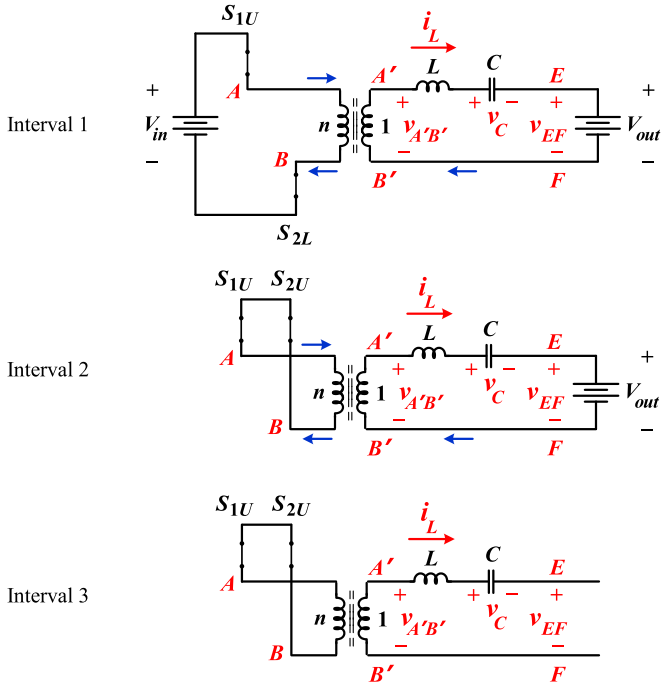

Fig. 5. Equivalent circuits for a half-cycle of DCM.

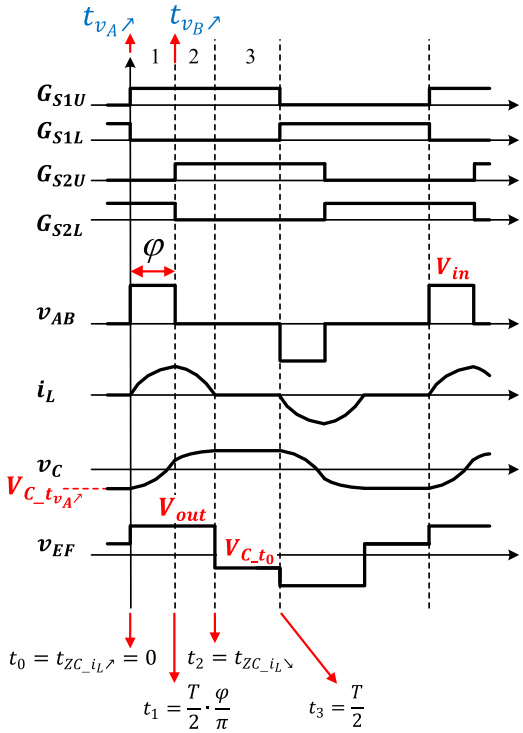

Fig. 6. Major voltage and current waveforms for DCM.

Both i_L and v_C increase toward positive values

$$\begin{bmatrix} Z_0 i_L(t) \\ v_C(t) \end{bmatrix} = \begin{bmatrix} -\sin\omega_0 t \\ \cos\omega_0 t \end{bmatrix} V_{\mathrm{Ct0}} + \begin{bmatrix} \sin\omega_0 t \\ 1-\cos\omega_0 t \end{bmatrix} \left(\frac{V_{\mathrm{in}}}{n} - V_{\mathrm{out}}\right) \tag{33}$$

with ω_0 and Z_0 defined in (1). This interval terminates at $t_1 = \frac{T}{2} \times \frac{\varphi}{\pi}$ when the rising (falling) edge of G_{S2U} (G_{S2L}) happens. At this moment, i_L and v_C reach I_{Lt1} and V_{Ct1}, by inserting $t = \frac{T}{2} \times \frac{\varphi}{\pi}$ in (33)

$$\begin{bmatrix} Z_0 I_{L\_t1} \\ V_{C\_t1} \end{bmatrix} = \begin{bmatrix} -\sin\omega_0 \left(\frac{T\varphi}{2\pi}\right) \\ \cos\omega_0 \left(\frac{T\varphi}{2\pi}\right) \end{bmatrix} V_{C\_t0} + \begin{bmatrix} \sin\omega_0 \left(\frac{T\varphi}{2\pi}\right) \\ 1-\cos\omega_0 \left(\frac{T\varphi}{2\pi}\right) \end{bmatrix} (1-M)\frac{V_{\mathrm{in}}}{n}. \quad (34)$$

2) Interval 2: $\frac{T}{2} \times \frac{\varphi}{\pi} \le t \le t_{\mathrm{ZCi_L}\searrow}$*:* During interval 2, $v_{A'B'}$ is zero while v_{EF} is still equal to V_{out}, as depicted in Fig. 5. At the beginning of this interval, i_L is at its maximum and then decreases, however v_C continues to rise

$$\begin{bmatrix} Z_0 i_L(t) \\ v_C(t) \end{bmatrix} = \begin{bmatrix} \cos\omega_0 t' & -\sin\omega_0 t' \\ \sin\omega_0 t' & \cos\omega_0 t' \end{bmatrix} \begin{bmatrix} Z_0 I_{\mathrm{Lt1}} \\ V_{\mathrm{Ct1}} \end{bmatrix} - \begin{bmatrix} \sin\omega_0 t' \\ 1-\cos\omega_0 t' \end{bmatrix} V_{\mathrm{out}} \quad (35)$$

where $t' = t - \frac{T}{2} \times \frac{\varphi}{\pi}$. This interval finishes at $t_2 = t_{\mathrm{ZCi_L}\searrow}$ when the i_L reaches to zero and v_C reaches to V_{Ct_2}

$$V_{C\_t2} = \left[\sin\omega_0 \left(t_{\mathrm{ZCi_L}\searrow} - \frac{T}{2}\cdot\frac{\varphi}{\pi}\right) \cos\omega_0 \left(t_{\mathrm{ZCi_L}\searrow} - \frac{T}{2}\cdot\frac{\varphi}{\pi}\right)\right] \times \begin{bmatrix} Z_0 I_{L\_t1} \\ V_{C\_t1} \end{bmatrix} - \left[1-\cos\omega_0 \left(t_{\mathrm{ZCi_L}\searrow} - \frac{T}{2}\cdot\frac{\varphi}{\pi}\right)\right] M\frac{V_{\mathrm{in}}}{n}. \quad (36)$$

3) Interval 3: $t_{\mathrm{ZCi_L}\searrow} \le t \le \frac{T}{2}$*:* Immediately after $t_{\mathrm{ZCi_L}\searrow}$, the rectifier diodes turn off and v_{EF} drops to V_{Ct_2}. This is equal to the capacitor voltage; thus, the inductor voltage is zero and i_L remains at zero. v_C remains equal to V_{Ct_2}. $v_{A'B'}$ is zero as well

$$\begin{bmatrix} Z_0 i(t) \\ v(t) \end{bmatrix} = \begin{bmatrix} 0 \\ V_{\mathrm{Ct2}} \end{bmatrix}. \quad (37)$$

This interval is finished by falling (rising) edge of G_{S1U} (G_{S1L}) at $t_3 = T/2$ where i_L and v_C reach to negative of their values at $t = 0$

$$\begin{bmatrix} Z_0 I_{\mathrm{Lt3}} \\ V_{\mathrm{Ct3}} \end{bmatrix} = \begin{bmatrix} 0 \\ V_{Ct_2} \end{bmatrix} = -\begin{bmatrix} Z_0 I_{\mathrm{Lt0}} \\ V_{\mathrm{Ct0}} \end{bmatrix}. \quad (38)$$

Using (33) to (38), we obtain $V_{\mathrm{Ct0DCM}} = V_{Ct_{v_A}\nearrow\mathrm{DCM}}$ and $t_{\mathrm{ZCi_L}\searrow\mathrm{DCM}}$ as

$$V_{C\_t_{v_A}\nearrow\_\mathrm{DCM}} = -\frac{(1-M)\sin^2\frac{\varphi}{2r}}{M-\sin^2\frac{\varphi}{2r}} \cdot \frac{V_{\mathrm{in}}}{n} \quad (39)$$

$$t_{\mathrm{ZC\_i_L}\searrow\_\mathrm{DCM}} = \frac{T}{2}\times\frac{\varphi}{\pi} + \frac{2}{\omega_0}\tan^{-1}\frac{2M(1-M)\sin\frac{\varphi}{r}}{(2M^2-2M+1)\cos\frac{\varphi}{r}-1+2M}. \quad (40)$$

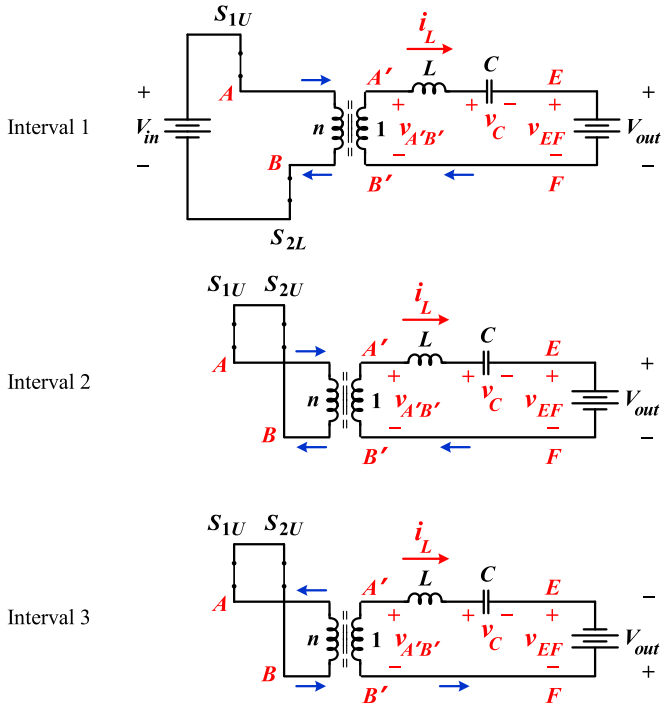

Fig. 7. Equivalent circuits for a half-cycle of CCM1.

And $t_{\mathrm{ZCi_L}\nearrow\mathrm{DCM}}$ is zero which is expected in the DCM. The active power is

$$P_{\mathrm{DCM}}(r, M, \varphi) = P_{\mathrm{base}} \times \frac{rM(1-M)\sin^2\frac{\varphi}{2r}}{\pi\left(M-\sin^2\frac{\varphi}{2r}\right)}. \quad (41)$$

B. CCM1

Similarly, there are three intervals in each half-cycle of SRC operating at CCM1 and the equivalent circuits for them are depicted in Fig. 7 with the typical voltage and current waveforms shown in Fig. 8. In this mode, the value of $I_{Lt_{v_A}\nearrow}$ is positive. This means that $t_{\mathrm{ZCi_L}\nearrow} < 0$.

1) Interval 1: $0 \le t \le \frac{T}{2} \times \frac{\varphi}{\pi}$*:* The switching cycle starts with interval 1 at the rising (falling) edge of G_{S1U} (G_{S1L}). At $t_0 = 0$, the initial values for i_L and v_C are $I_{\mathrm{Lt0}} > 0$ and $V_{\mathrm{Ct0}} < 0$, respectively. $v_{A'B'}$ is equal to V_{in}/n and v_{EF} is equal to V_{out}. Both i_L and v_C increase toward positive values

$$\begin{bmatrix} Z_0 i_L(t) \\ v_C(t) \end{bmatrix} = \begin{bmatrix} \cos\omega_0 t & -\sin\omega_0 t \\ \sin\omega_0 t & \cos\omega_0 t \end{bmatrix} \begin{bmatrix} Z_0 I_{\mathrm{Lt0}} \\ V_{\mathrm{Ct0}} \end{bmatrix} + \begin{bmatrix} \sin\omega_0 t \\ 1-\cos\omega_0 t \end{bmatrix} \left(\frac{V_{\mathrm{in}}}{n} - V_{\mathrm{out}}\right). \quad (42)$$

This interval terminates at $t_1 = \frac{T}{2} \times \frac{\varphi}{\pi}$ when the rising (falling) edge of G_{S2U} (G_{S2L}) happens. At this moment, i_L

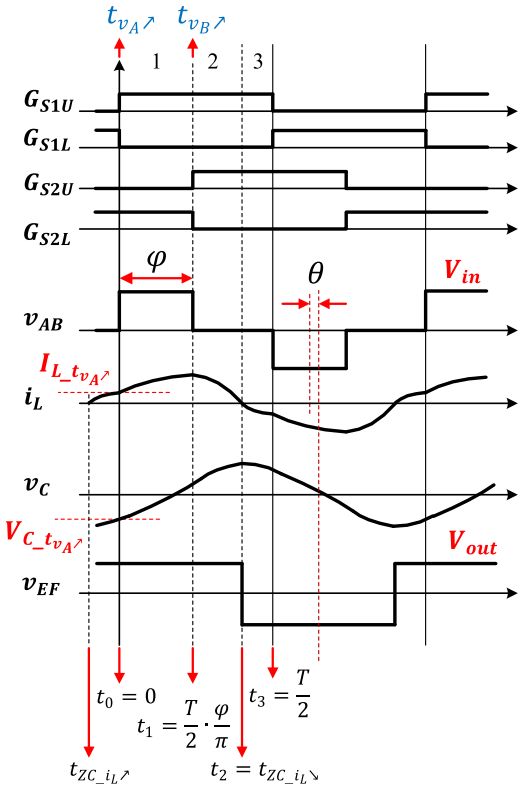

Fig. 8. Major voltage and current waveforms for CCM1.

and v_C reach I_{Lt1} and V_{Ct1}, by inserting $t = \frac{T}{2} \times \frac{\varphi}{\pi}$ in (42)

$$\begin{bmatrix} Z_0 I_{L\_t1} \\ V_{C\_t1} \end{bmatrix} = \begin{bmatrix} \cos\omega_0\left(\frac{T}{2}\cdot\frac{\varphi}{\pi}\right) & -\sin\omega_0\left(\frac{T}{2}\cdot\frac{\varphi}{\pi}\right) \\ \sin\omega_0\left(\frac{T}{2}\cdot\frac{\varphi}{\pi}\right) & \cos\omega_0\left(\frac{T}{2}\cdot\frac{\varphi}{\pi}\right) \end{bmatrix} \begin{bmatrix} Z_0 I_{L\_t0} \\ V_{C\_t0} \end{bmatrix} + \begin{bmatrix} \sin\omega_0\left(\frac{T}{2}\cdot\frac{\varphi}{\pi}\right) \\ 1-\cos\omega_0\left(\frac{T}{2}\cdot\frac{\varphi}{\pi}\right) \end{bmatrix} (1-M)\frac{V_{\mathrm{in}}}{n}. \quad (43)$$

The symbol θ in Fig. 8 represents the phase difference between the symmetry axes of v_{AB} and v_{EF}.

2) Interval 2: $\frac{T}{2} \times \frac{\varphi}{\pi} \le t \le t_{\mathrm{ZCi_L}\searrow}$: During interval 2, $v_{A'B'}$ is zero while v_{EF} is still equal to V_{out}, as depicted in Fig. 7. i_L reduces but v_C rises

$$\begin{bmatrix} Z_0 i_L(t) \\ v_C(t) \end{bmatrix} = \begin{bmatrix} \cos\omega_0 t' & -\sin\omega_0 t' \\ \sin\omega_0 t' & \cos\omega_0 t' \end{bmatrix} \begin{bmatrix} Z_0 I_{\mathrm{Lt1}} \\ V_{\mathrm{Ct1}} \end{bmatrix} - \begin{bmatrix} \sin\omega_0 t' \\ 1-\cos\omega_0 t' \end{bmatrix} V_{\mathrm{out}} \quad (44)$$

with $t' = t - \frac{T}{2}\cdot\frac{\varphi}{\pi}$. This interval terminates at the moment when i_L reaches to zero, denoted by $t_{\mathrm{ZCi_L}\searrow}$ which also satisfies the relation $t_{\mathrm{ZCi_L}\searrow} = t_{\mathrm{ZCi_L}\nearrow} + \frac{T}{2}$. At this moment, i_L and v_C reach to I_{Lt2} and V_{Ct2}, by inserting $t = t_{\mathrm{ZCi_L}\searrow}$ in (44)

$$V_{C\_t2} = \left[\sin\omega_0\left(t_{\mathrm{ZC\_i_L}\searrow} - \frac{T}{2}\cdot\frac{\varphi}{\pi}\right)\cos\omega_0\left(t_{\mathrm{ZC\_i_L}\searrow} - \frac{T}{2}\cdot\frac{\varphi}{\pi}\right)\right] \times \begin{bmatrix} Z_0 I_{L\_t1} \\ V_{C\_t1} \end{bmatrix} - \left[1-\cos\omega_0\left(t_{\mathrm{ZC\_i_L}\searrow} - \frac{T}{2}\cdot\frac{\varphi}{\pi}\right)\right] M\frac{V_{\mathrm{in}}}{n}. \quad (45)$$

3) Interval 3: $t_{\mathrm{ZCi_L}\searrow} \le t \le \frac{T}{2}$: Immediately after $t_{\mathrm{ZCi_L}\searrow}$, v_{EF} drops to $-V_{\mathrm{out}}$. i_L becomes negative and v_C reduces. $v_{A'B'}$ remains at zero

$$\begin{bmatrix} Z_0 i_L(t) \\ v_C(t) \end{bmatrix} = \begin{bmatrix} -\sin\omega_0 t'' \\ \cos\omega_0 t'' \end{bmatrix} V_{\mathrm{Ct2}} + \begin{bmatrix} \sin\omega_0 t'' \\ 1-\cos\omega_0 t'' \end{bmatrix} V_{\mathrm{out}} \quad (46)$$

where t'' is $t - t_{\mathrm{ZCi_L}\searrow}$. By of falling (rising) edge of G_{S1U} (G_{S1L}) at $t_3 = T/2$, this interval is finished. At this moment, i_L and v_C reach to negative of their values at $t = 0$

$$\begin{bmatrix} Z_0 I_{L\_t3} \\ V_{C\_t3} \end{bmatrix} = \begin{bmatrix} -\sin\omega_0\left(\frac{T}{2} - t_{\mathrm{ZC\_i_L}\searrow}\right) \\ \cos\omega_0\left(\frac{T}{2} - t_{\mathrm{ZC\_i_L}\searrow}\right) \end{bmatrix} V_{C\_t2} + \begin{bmatrix} \sin\omega_0\left(\frac{T}{2} - t_{\mathrm{ZC\_i_L}\searrow}\right) \\ 1-\cos\omega_0\left(\frac{T}{2} - t_{\mathrm{ZC\_i_L}\searrow}\right) \end{bmatrix} M\frac{V_{\mathrm{in}}}{n}. \quad (47)$$

Due to half-cycle antisymmetry, we have

$$\begin{bmatrix} Z_0 I_{\mathrm{Lt3}} \\ V_{\mathrm{Ct3}} \end{bmatrix} = -\begin{bmatrix} Z_0 I_{\mathrm{Lt0}} \\ V_{\mathrm{Ct0}} \end{bmatrix}. \quad (48)$$

To find three unknowns I_{Lt0}, V_{Ct0}, and $t_{\mathrm{ZCi_L}\searrow}$, we use (42)–(48) and find

$$I_{L\_t0\_CCM1} = -\frac{1}{Z_0\cos\frac{\pi}{2r}}\left\{\sin\frac{\varphi}{2r}\cos\left(\frac{\pi}{2r} - \frac{\varphi}{2r}\right) + M\sin\left(\frac{\pi}{2r} - \omega_0 t_{\mathrm{ZC\_i_L}\searrow\_CCM1}\right)\right\}\cdot\frac{V_{\mathrm{in}}}{n} \quad (49)$$

$$V_{C\_t0\_CCM1} = -\frac{1}{\cos\frac{\pi}{2r}}\left\{\sin\frac{\varphi}{2r}\sin\left(\frac{\pi}{2r} - \frac{\varphi}{2r}\right) + M\left[\cos\frac{\pi}{2r} - \cos\left(\frac{\pi}{2r} - \omega_0 t_{\mathrm{ZC\_i_L}\searrow\_CCM1}\right)\right]\right\}\cdot\frac{V_{\mathrm{in}}}{n} \quad (50)$$

whereas $t_{\mathrm{ZCi_L}\searrow\mathrm{CCM1}}$ is

$$t_{\mathrm{ZC\_i_L}\searrow\_CCM1} = \frac{1}{\omega_0}\left\{\frac{\pi}{2r} + \frac{\varphi}{2r} + \cos^{-1}\left[M\frac{\sin\left(\frac{\pi}{2r}\right)}{\sin\left(\frac{\varphi}{2r}\right)}\right]\right\} > 0. \quad (51)$$

Here, we rename I_{Lt0CCM1} as $I_{Lt_{v_A}\nearrow\mathrm{CCM1}}$ and V_{Ct0CCM1} as $V_{Ct_{v_A}\nearrow\mathrm{CCM1}}$ to clearly state their importance in the ZVS of the leading leg. Thus

$$I_{L\_t_{v_A}\nearrow\_CCM1} = I_{\mathrm{base}}\frac{-1}{\pi\cos\frac{\pi}{2r}}\left\{\sin\frac{\varphi}{2r}\cos\left(\frac{\pi}{2r} - \frac{\varphi}{2r}\right) - M\sin\left(\frac{\varphi}{2r} + \cos^{-1}\left[M\frac{\sin\left(\frac{\pi}{2r}\right)}{\sin\left(\frac{\varphi}{2r}\right)}\right]\right)\right\}. \quad (52)$$

Knowing $t_{\mathrm{ZCi_L}\searrow} = t_{\mathrm{ZCi_L}\nearrow} + \frac{T}{2}$, we get

$$t_{\mathrm{ZCi_L}\nearrow \mathrm{CCM1}} = \frac{1}{\omega_0}\left\{-\frac{\pi}{2r} + \frac{\varphi}{2r} + \cos^{-1}\left[M\frac{\sin\left(\frac{\pi}{2r}\right)}{\sin\left(\frac{\varphi}{2r}\right)}\right]\right\} < 0. \tag{53}$$

Having $I_{Lt_{v_\mathrm{A}}\nearrow \mathrm{CCM1}} > 0$ is equivalent to the lack of ZVS for the leading leg transition, $v_\mathrm{A}\nearrow$.

Parameter θ is found to be

$$\theta_{\mathrm{CCM1}} = r\cos^{-1}\left[M\frac{\sin\left(\frac{\pi}{2r}\right)}{\sin\left(\frac{\varphi}{2r}\right)}\right]. \tag{54}$$

The active power is

$$P_{\mathrm{CCM1}}(r, M, \varphi) = P_{\mathrm{base}} \times \frac{rM}{\pi\cos\frac{\pi}{2r}}\sqrt{\sin^2\frac{\varphi}{2r} - M^2\sin^2\frac{\pi}{2r}}. \tag{55}$$

As the values of $I_{Lt_{v_\mathrm{A}}\nearrow \mathrm{CCM1}}$ in this mode are positive, it is possible to find the point where its maximum occurs, by substituting $t_{\mathrm{ZCi_L}\searrow \mathrm{CCM1}}$ from (51) in (49). The maximum $I_{Lt_{v_\mathrm{A}}\nearrow \mathrm{CCM1}}$ occurs at

$$\begin{aligned}\varphi_{I_{L\_t_{v_\mathrm{A}}\nearrow\_\max}} &= (2-r)\frac{\pi}{3}\\ M_{I_{L\_t_{v_\mathrm{A}}\nearrow\_\max}} &= \frac{\sin\frac{(2-r)\pi}{6r}}{\sqrt{2}\sin\frac{\pi}{2r}}\sqrt{1+\sin\frac{(2-r)\pi}{6r}}.\end{aligned} \tag{56}$$

Note that here in contrary to the prediction of FHA the location of this maximum current point directly changes with r. The value of $I_{L\_t_{v_\mathrm{A}}\nearrow\_\max}$ can be found by substituting $\varphi = \varphi_{I_{L\_t_{v_\mathrm{A}}\nearrow\_\max}}$ and $M = M_{I_{L\_t_{v_\mathrm{A}}\nearrow\_\max}}$ into (49).

CCM1 mode does not necessarily occur for any combination of (r, M, φ). The condition is provided later in the paper.

C. Continuous Current Mode 2 (CCM2)

There are three intervals in each half cycle of SRC operating at CCM2 with the equivalent circuits in Fig. 9 and the typical voltage and current waveforms in Fig. 10. In this mode, $I_{Lt_{v_\mathrm{A}}\nearrow}$ is negative. Therefore, $t_{\mathrm{ZCi_L}\nearrow} > 0$.

1) Interval 1: $0 \le t \le t_{\mathrm{ZCi_L}\nearrow}$: The start of switching cycle with interval 1 is at the moment of rising (falling) edge of $G_{S1U}(G_{S1L})$. At $t_0 = 0$, the initial values for i_L and v_C are $I_{L-t_0} < 0$ and $V_{C-t_0} < 0$, respectively. $v_{A'B'}$ and v_{EF} are V_{in}/n and $-V_{\mathrm{out}}$, respectively. i_L increases toward positive values but v_C still gets more negative. The state equation is

$$\begin{bmatrix} Z_0 i_L(t) \\ v_C(t)\end{bmatrix} = \begin{bmatrix}\cos\omega_0 t & -\sin\omega_0 t \\ \sin\omega_0 t & \cos\omega_0 t\end{bmatrix}\begin{bmatrix} Z_0 I_{L\_t0} \\ V_{C\_t0}\end{bmatrix} + \begin{bmatrix}\sin\omega_0 t \\ 1-\cos\omega_0 t\end{bmatrix}\left(\frac{V_{\mathrm{in}}}{n} + V_{\mathrm{out}}\right). \tag{57}$$

At $t_1 = t_{\mathrm{ZCi_L}\nearrow}$, this interval finishes when i_L reaches to zero. v_C is V_{Ct1}, by inserting $t = t_{\mathrm{ZCi_L}\nearrow}$ in (57)

$$V_{C\_t1} = \begin{bmatrix}\sin\omega_0 t_{\mathrm{ZC\_i_L}\nearrow} & \cos\omega_0 t_{\mathrm{ZC\_i_L}\nearrow}\end{bmatrix}\begin{bmatrix} Z_0 I_{L\_t0} \\ V_{C\_t0}\end{bmatrix} + (1-\cos\omega_0 t_{\mathrm{ZC\_i_L}\nearrow})(1+M)\frac{V_{\mathrm{in}}}{n}. \tag{58}$$

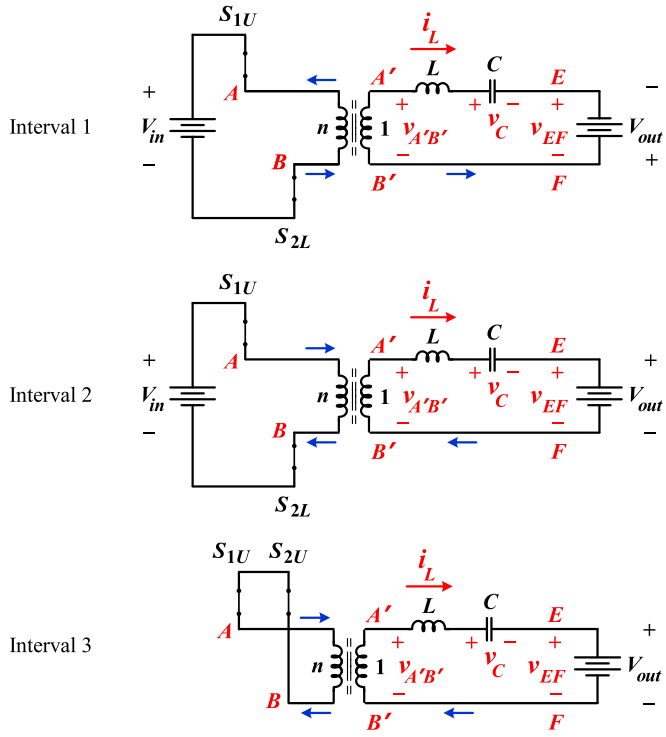

Fig. 9. Equivalent circuits for a half-cycle of CCM2.

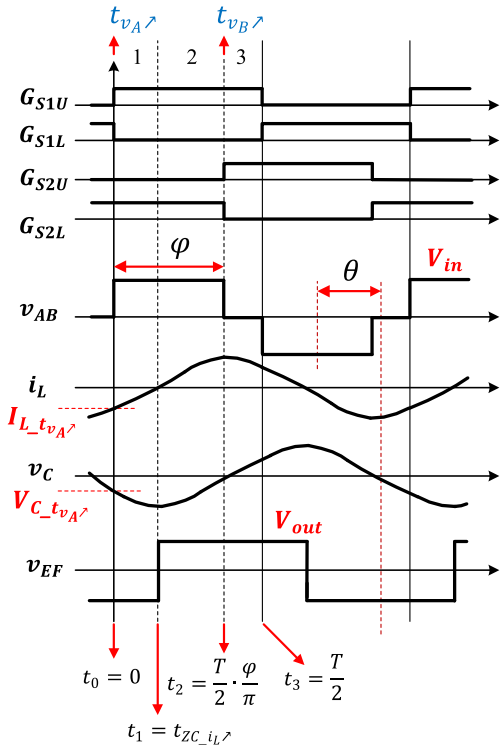

Fig. 10. Major voltage and current waveforms for CCM2.

2) Interval 2: $t_{\mathrm{ZCi_L}\nearrow} \le t \le \frac{T}{2} \times \frac{\varphi}{\pi}$*:* After $t_{\mathrm{ZCi_L}\nearrow}$, v_{EF} jumps to V_{out} and $v_{A'B'}$ remains at V_{in}/n. i_L becomes positive and v_C starts rising toward positive values

$$\begin{bmatrix} Z_0 i_L\,(t) \\ v_C\,(t) \end{bmatrix} = \begin{bmatrix} -\sin\omega_0 t' \\ \cos\omega_0 t' \end{bmatrix} V_{C\_t1} + \begin{bmatrix} \sin\omega_0 t' \\ 1-\cos\omega_0 t' \end{bmatrix} \left(\frac{V_{\mathrm{in}}}{n} - V_{\mathrm{out}}\right) \quad (59)$$

where $t' = t - t_{\mathrm{ZCi_L}\nearrow}$. This interval finishes at rising (falling) edge of G_{S1U} (G_{S1L}) at $t_2 = \frac{T}{2} \times \frac{\varphi}{\pi}$. i_L and v_C are I_{Lt2} and V_{Ct2}, respectively, by inserting $t = \frac{T}{2} \times \frac{\varphi}{\pi}$ in (59)

$$\begin{bmatrix} Z_0 I_{L\_t2} \\ V_{C\_t2} \end{bmatrix} = \begin{bmatrix} -\sin\omega_0\left(\frac{T}{2}\cdot\frac{\varphi}{\pi} - t_{\mathrm{ZC\_i_L}\nearrow}\right) \\ \cos\omega_0\left(\frac{T}{2}\cdot\frac{\varphi}{\pi} - t_{\mathrm{ZC\_i_L}\nearrow}\right) \end{bmatrix} V_{C\_t1} + \begin{bmatrix} \sin\omega_0\left(\frac{T}{2}\cdot\frac{\varphi}{\pi} - t_{\mathrm{ZC\_i_L}\nearrow}\right) \\ 1-\cos\omega_0\left(\frac{T}{2}\cdot\frac{\varphi}{\pi} - t_{\mathrm{ZC\_i_L}\nearrow}\right) \end{bmatrix} \times (1-M)\frac{V_{\mathrm{in}}}{n}. \quad (60)$$

3) Interval 3: $\frac{T}{2} \times \frac{\varphi}{\pi} \le t \le \frac{T}{2}$*:* During interval 3, $v_{A'B'}$ is zero while $v_{\mathrm{EF}}$is equal to V_{out}. i_L reduces but v_C rises

$$\begin{bmatrix} Z_0 i_L\,(t) \\ v_C\,(t) \end{bmatrix} = \begin{bmatrix} \cos\omega_0 t'' & -\sin\omega_0 t'' \\ \sin\omega_0 t'' & \cos\omega_0 t'' \end{bmatrix} \times \begin{bmatrix} Z_0 I_{L\_t2} \\ V_{C\_t2} \end{bmatrix} - \begin{bmatrix} \sin\omega_0 t'' \\ 1-\cos\omega_0 t'' \end{bmatrix} V_{\mathrm{out}} \quad (61)$$

where $t'' = t - \frac{T}{2} \times \frac{\varphi}{\pi}$.

This interval terminates at $t_3 = T/2$ when the falling (rising) edge of (G_{S1U} G_{S1L}) happens

$$\begin{bmatrix} Z_0 I_{L\_t3} \\ V_{C\_t3} \end{bmatrix} = \begin{bmatrix} \cos\omega_0\left(\frac{T}{2} - \frac{T}{2}\cdot\frac{\varphi}{\pi}\right) & -\sin\omega_0\left(\frac{T}{2} - \frac{T}{2}\cdot\frac{\varphi}{\pi}\right) \\ \sin\omega_0\left(\frac{T}{2} - \frac{T}{2}\cdot\frac{\varphi}{\pi}\right) & \cos\omega_0\left(\frac{T}{2} - \frac{T}{2}\cdot\frac{\varphi}{\pi}\right) \end{bmatrix} \times \begin{bmatrix} Z_0 I_{L\_t2} \\ V_{C\_t2} \end{bmatrix} - \begin{bmatrix} \sin\omega_0\left(\frac{T}{2} - \frac{T}{2}\cdot\frac{\varphi}{\pi}\right) \\ 1-\cos\omega_0\left(\frac{T}{2} - \frac{T}{2}\cdot\frac{\varphi}{\pi}\right) \end{bmatrix} M\frac{V_{\mathrm{in}}}{n}. \quad (62)$$

At $t_3 = T/2$, i_L and v_C reach to negative of their values at $t = 0$

$$\begin{bmatrix} Z_0 I_{\mathrm{Lt3}} \\ V_{\mathrm{Ct3}} \end{bmatrix} = -\begin{bmatrix} Z_0 I_{\mathrm{Lt0}} \\ V_{\mathrm{Ct0}} \end{bmatrix}. \quad (63)$$

To find three unknowns I_{Lt0}, V_{Ct0}, and $t_{\mathrm{ZCi_L}\nearrow}$, we use (57)–(63) to obtain

$$I_{L\_t0\_\mathrm{CCM2}} = -\frac{1}{Z_0\cos\frac{\pi}{2r}}\left\{\sin\frac{\varphi}{2r}\cos\left(\frac{\pi}{2r} - \frac{\varphi}{2r}\right) - M\sin\left(\frac{\pi}{2r} - \omega_0 t_{\mathrm{ZC\_i_L}\nearrow\_\mathrm{CCM2}}\right)\right\}\cdot\frac{V_{\mathrm{in}}}{n} \quad (64)$$

$$V_{C\_t0\_\mathrm{CCM2}} = -\frac{1}{\cos\frac{\pi}{2r}}\left\{\sin\frac{\varphi}{2r}\sin\left(\frac{\pi}{2r} - \frac{\varphi}{2r}\right) - M\left[\cos\frac{\pi}{2r} - \cos\left(\frac{\pi}{2r} - \omega_0 t_{\mathrm{ZC\_i_L}\nearrow\_\mathrm{CCM2}}\right)\right]\right\}\cdot\frac{V_{\mathrm{in}}}{n} \quad (65)$$

whereas $t_{\mathrm{ZCi_L}\nearrow\mathrm{CCM2}}$ is

$$t_{\mathrm{ZCi_L}\nearrow\mathrm{CCM2}} = \frac{1}{\omega_0}\left\{\frac{\varphi}{2r} - \sin^{-1}\left[\frac{M\sin\frac{\pi}{2r}}{\cos\left(\frac{\pi}{2r} - \frac{\varphi}{2r}\right)}\right]\right\}. \quad (66)$$

Again we rename I_{Lt0CCM2} as $I_{Lt_{v_\mathrm{A}}\nearrow\mathrm{CCM2}}$ and V_{Ct0CCM2} as $V_{Ct_{v_\mathrm{A}}\nearrow\mathrm{CCM2}}$ to show their importance in the ZVS of the leading leg. Thus

$$I_{L\_t_{v_\mathrm{A}}\nearrow\_\mathrm{CCM2}} = I_{\mathrm{base}}\frac{-1}{\pi\cos\frac{\pi}{2r}}\sin\frac{\varphi}{2r}\cos\left(\frac{\pi}{2r} - \frac{\varphi}{2r}\right) + I_{\mathrm{base}}\frac{M}{\pi\cos\frac{\pi}{2r}}\sin\left(\frac{\pi}{2r} - \frac{\varphi}{2r} + \sin^{-1}\left[\frac{M\sin\frac{\pi}{2r}}{\cos\left(\frac{\pi}{2r} - \frac{\varphi}{2r}\right)}\right]\right). \quad (67)$$

From $t_{\mathrm{ZCi_L}\searrow} = t_{\mathrm{ZCi_L}\nearrow} - \frac{T}{2}$, we can get $t_{\mathrm{ZCi_L}\searrow}$. Parameter θ is

$$\theta_{\mathrm{CCM2}} = \frac{\pi}{2} - r\sin^{-1}\left[\frac{M\sin\frac{\pi}{2r}}{\cos\left(\frac{\pi}{2r} - \frac{\varphi}{2r}\right)}\right]. \quad (68)$$

The active power is

$$P_{\mathrm{CCM2}}\,(r, M, \varphi) = P_{\mathrm{base}}\frac{rM}{\pi\cos\frac{\pi}{2r}} \times \left[\sqrt{\cos^2\left(\frac{\pi}{2r} - \frac{\varphi}{2r}\right) - M^2\sin^2\frac{\pi}{2r}} - \cos\frac{\pi}{2r}\right]. \quad (69)$$

The maximum power for a specific (M, r) happens when φ is the largest. After substituting $\varphi = \pi$ in (55) and differentiating

$M_{P_{\max}}$ is found as

$$M_{P_{\max\_CCM2}} = \frac{X}{2\sqrt{2}\sin\frac{\pi}{2r}}$$
$$X = \sqrt{4-\cos^2\frac{\pi}{2r}-\cos\frac{\pi}{2r}\sqrt{\cos^2\frac{\pi}{2r}+8}}\,. \tag{70}$$

The value of $P_{\max}$ can be found by substituting $\varphi = \pi$ and $M = M_{P_{\max}}$ into (69). In contrary to the case of FHA, the location of this maximum power point changes directly with r. The load resistance at this point is

$$R_{LP_{\max\_CCM2}} = \frac{\pi}{2r}\cot\frac{\pi}{2r} \times \frac{X}{\sqrt{8-X^2}-2\sqrt{2}\cos\frac{\pi}{2r}}Z_0 \tag{71}$$

with X introduced in (70).

Similar to the case of (18), the time-domain analysis can predict M in each mode as a function of V_{in} and R_L. Using Q from (16), we define parameter k as

$$k = \frac{4Q}{\pi r} = \frac{\pi}{2r} \times \frac{Z_0}{R_L}. \tag{72}$$

By substituting P_{base} from (17) in (41), (55), and (69), M in each mode can be calculated as

$$M_{\text{DCM}} = \frac{1}{2k^2}\left[(1-k)^2\left(\sin^2\frac{\varphi}{2r}\right)^2 + k\right]\sin^2\frac{\varphi}{2r} \tag{73}$$

$$M_{\text{CCM1}} = \frac{1}{\sqrt{k^2\cot^2\frac{\pi}{2r}+1}} \tag{74}$$

$$M_{\text{CCM2}} = \frac{-k+\sqrt{k^2+\left(k^2+\tan^2\frac{\pi}{2r}\right)\left(\cos^2\left(\frac{\pi}{2r}-\frac{\varphi}{2r}\right)-\cos^2\frac{\pi}{2r}\right)}}{k^2+\tan^2\frac{\pi}{2r}}. \tag{75}$$

Due to possibility of only one mode per each combination of φ, r, and R_L (through k), the calculated M from (73)–(75) should be examined with the criteria in Table II to find the correct M value as well as the mode at which the converter operates for this combination of φ, r, and R_L.

V. Mode Boundaries in Time-Domain Approach

A. DCM–CCM1 Boundary

The DCM–CCM1 boundary is the situation where the resonant capacitor voltage at $t = 0$, V_{Ct0}, becomes equal to the negative of the load voltage, $-V_{\text{out}}$. Substituting $V_{C\_t0} = -V_{\text{out}}$ into (39), we obtain the boundary phase shift $\varphi_{\text{DCM\_CCM1}}$ as

$$\varphi_{\text{DCM\_CCM1}}\ (r, M) = r\cos^{-1}\left(1-2M^2\right). \tag{76}$$

At this border line, the power is governed by (77) which is different than prediction of $P_{\text{DCM\_CCMH1}}\ (M) = 0$ in (20)

$$P_{\text{DCM\_CCM1}}\ (r, M) = P_{\text{base}} \times \frac{rM^2}{\pi}. \tag{77}$$

B. DCM–CCM2 Boundary

The DCM–CCM2 boundary is the case where $t_{\text{ZC\_i}_\text{L}\searrow\text{DCM}}$ in (40) reaches to $T/2$. Having $t_{\text{ZC\_i}_\text{L}\searrow\text{DCM}} = T/2$ in (40), we find the boundary phase shift $\varphi_{\text{DCM\_CCM2}}$ as

$$\varphi_{\text{DCM\_CCM2}}\ (r, M) = \frac{\pi}{2} + r\sin^{-1}\left[(2M-1)\sin\frac{\pi}{2r}\right]$$
$$M + \cos\frac{\pi}{r} > 0. \tag{78}$$

At this border line, the power is governed by

$$P_{\text{DCM\_CCM2}}\ (r, M) = P_{\text{base}}\frac{rM}{2\pi\cos\frac{\pi}{2r}} \times\left[\sqrt{1-\left[(2M-1)\sin\frac{\pi}{2r}\right]^2}-\cos\frac{\pi}{2r}\right] \tag{79}$$

for $1 > M > -\cos\frac{\pi}{r}$.

C. CCM1–CCM2 Boundary

The CCM1–CCM2 boundary is the situation $t_{\text{ZC\_i}_\text{L}\searrow\text{CCM1}}$ in (51) reaches to $T/2$. Substituting $I_{\text{Lt0}} = 0$ and $t_{\text{ZC\_i}_\text{L}\searrow\text{CCM1}} = T/2$ into (49), the boundary phase shift $\varphi_{\text{CCM1\_CCM2}}$ is calculated as

$$\varphi_{\text{CCM1\_CCM2}}\ (r, M) = \frac{\pi}{2} + r\sin^{-1}\left[(2M-1)\sin\frac{\pi}{2r}\right]$$
$$M + \cos\frac{\pi}{r} < 0. \tag{80}$$

At this border line, the power is given by

$$P_{\text{CCM1\_CCM2}}\ (r, M) = P_{\text{base}}\frac{rM}{2\pi\cos\frac{\pi}{2r}} \times\left[\sqrt{1-\left[(2M-1)\sin\frac{\pi}{2r}\right]^2}-\cos\frac{\pi}{2r}\right]$$
$$-\cos\frac{\pi}{r} > M > 0. \tag{81}$$

Similarity between predictions of (78) and (80) indicates that when CCM1 exists, CCM1–CCM2 boundary prevails DCM–CCM2 boundary.

Table I summarizes the boundary conditions between the three modes. Note that the criterion to distinguish between DCM–CCM2 and CCM1–CCM2 boundaries is provided in the rightmost column of Table I. Knowing M and r is sufficient to decide between the predictions of (78) and (80). Table II shows the criteria for each mode.

The boundaries predicted by time-domain analysis are visualized in Fig. 11 on the same (M, φ) plane as in Fig. 4. Both Fig. 4 and Fig. 11 predict that at $\varphi = \pi$ or the square waveform situation, the converter operates at CCM2 for all M values. This explains why in early days of SRC initial research using square wave and frequency modulation the CCM1 mode was not frequently reported. In contrary to FHA which did not predict any boundary between DCM and CCM2, the DCM–CCM2 boundaries predicted by time-domain analysis are evident in Fig. 11.

TABLE I
MODE BOUNDARY CONDITIONS AND FORMULA

Boundary	Condition	Formula	Criterion
DCM–CCM1	$V_{C\_0} = -V_{\text{out}}$	$\varphi_{\text{DCM\_CCM1}} = r\cos^{-1}(1-2M^2)$	–
DCM–CCM2	$i_L\,(T/2) = 0$	$\varphi_{\text{DCM\_CCM2}} = \frac{\pi}{2} + r\sin^{-1}\left[(2M-1)\sin\left(\frac{\pi}{2r}\right)\right]$	$-\cos\frac{\pi}{r} < M < 1$
CCM1–CCM2	$i_L\,(T/2) = 0$	$\varphi_{\text{CCM1\_CCM2}} = \frac{\pi}{2} + r\sin^{-1}\left[(2M-1)\sin\left(\frac{\pi}{2r}\right)\right]$	$0 < M < -\cos\frac{\pi}{r}$

TABLE II
CRITERIA FOR MODES

Mode	Criterion 1	Criterion 2
CCM2	$\frac{\pi}{2} + r\sin^{-1}\left[(2M-1)\sin\left(\frac{\pi}{2r}\right)\right] < \varphi$	–
CCM1	$r\cos^{-1}(1-2M^2) < \varphi < \frac{\pi}{2} + r\sin^{-1}\left[(2M-1)\sin\left(\frac{\pi}{2r}\right)\right]$	$-\cos\frac{\pi}{r} < M < 1$
DCM	$\varphi < \frac{\pi}{2} + r\sin^{-1}\left[(2M-1)\sin\left(\frac{\pi}{2r}\right)\right]$	$-\cos\frac{\pi}{r} < M < 1$
	$\varphi < r\cos^{-1}(1-2M^2)$	$0 < M < -\cos\frac{\pi}{r}$

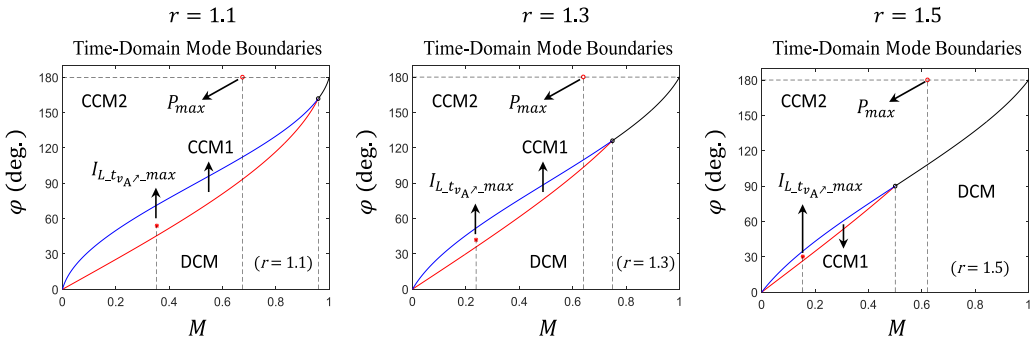

Fig. 11. Mode boundaries predicted by time-domain analysis for $r = 1.1, 1.3$, and 1.5. Points of $I_{L\_t_{v_A}\nearrow\_\max}$ in CCM1 and $P_{\max}$ in CCM2 are shown.

Similar to Fig. 4, the maximum $I_{L\_t_{v_A}\nearrow}$ point occurs in CCM1 and the maximum power point happens in CCM2. The boundaries and maximum points are explicitly dependent of parameter r as given in Table I. The extra criterion on M distinguished between DCM–CCM2 and CCM1–CCM2 boundaries that have the same formula.

In general, the area of CCM1 region in Fig. 11 is less than the similar area in Fig. 4 and at higher r the gets smaller. The readers are encouraged to run the accompanied "SRC_Modes" calculator described in the Appendix.

A triple-point is the only operating condition where are three modes coexist. At the triple point $\varphi_{\text{CCM1\_CCM2}}$ and $\varphi_{\text{DCM\_CCM1}}$ are equal; thus, using (76) and (80), we obtain

$$M_{\text{triple\_point}} = -\cos\frac{\pi}{r},\quad \varphi_{\text{triple\_point}} = \pi\,(2-r)\,. \tag{82}$$

Figs. 12 and 13 illustrate the locus of triple points, as $M_{\text{triple\_point}}$ and $\varphi_{\text{triple\_point}}$ versus r. In both figures, the locus separates the region with all three modes (below the curve) from the region with only DCM and CCM2. Knowing two of φ, M, and r is sufficient to have the entire behavior of SRC, mode of operation, possibility of having CCM1, and the soft-switching condition. And it is not necessary to use power levels to know the mode boundaries, as suggested in [44].

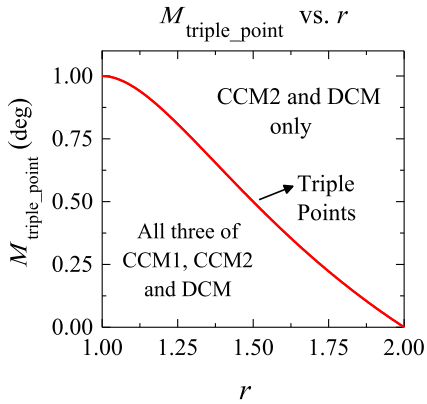

Fig. 12. M versus r with triple points.

In the next section, the numerical predictions of FHA and the time-domain approaches for key quantities are cross-examined in detail.

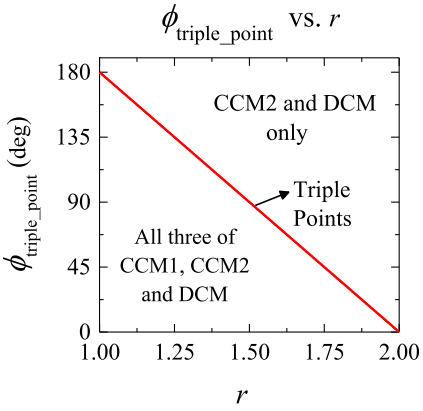

Fig. 13. φ versus r with triple points.

VI. Comparison of FHA and Time-Domain Analysis Approaches

This section provides an objective comparison between the predictions of the same converter under FHA and with time-domain methods. All the values are represented as normalized using base values given in (7) and (10).

The first harmonic approximation assumes the current in the resonant tank to be sinusoidal with the frequency equal to the switching frequency. Due to the continuous nature of a sinusoidal waveform, FHA cannot provide insight for the quantities in DCM mode. Also FHA does not differentiate between CCM1 and CCM2. The first row of Fig. 14 shows the normalized power predicted in (9) for $r = 1.1$, 1.3, and 1.5. Under FHA, the locations of the maximum current point and the maximum power point, given in (25) and (28), respectively, do not depend on r.

Time-domain analysis explains both the continuous and discontinuous modes. The second row of Fig. 14 shows the power predicted in (41), (55), and (69) for the same three r values. Similar to FHA, the maximum power point occurs at $\varphi = \pi$ in CCM2, predicted in (70), depends explicitly on r and shifts to lower M numbers at higher r values. The third row of Fig. 14 shows the difference between power predictions. For majority of (M, φ) plane, FHA predicts a higher power which can reach up to 28% of excessive power estimation.

Fig. 15 illustrates the normalized maximum current predictions of FHA and time-domain approaches which are important factors in selecting the semiconductors of the circuit. Both the methods evaluate similar currents for a short circuit ($M = 0$) with square waveform voltage ($\varphi = \pi$). Also, in both methods, the current reaches zero at $M = 1$ which is compatible with the SRC accepted as a step-down converter (neglecting an anomalous step-up operation reported in [46]). Similar to the case of power, generally FHA has higher maximum current predictions that reach up to 35% of difference.

Knowledge of RMS current is required for thermal design of the converter. Fig. 16 depicts the normalized RMS current predictions of FHA and time-domain approaches. Similar to the case of maximum current, both methods find similar currents for $M = 0$ and $\varphi = \pi$. Again FHA predicts larger RMS that reach up to 20% of difference. Comparing Fig. 15 with Fig. 16 shows that the regions of overestimation or underestimation have different patterns for $I_{L\_\max}$ and I_{L_rms}.

Fig. 17 shows the normalized maximum voltage across the resonant capacitance which is required to select the correct capacitor rating. As expected, the highest voltage occurs at lower r with $M = 0$ and $\varphi = \pi$, which is the situation of highest current passing through the resonant capacitor. At this point, the capacitor voltage can reach up to six times the dc voltage. This can be important to select the capacitor with correct voltage margins if the short circuit events are expected to be frequent for the converter. Again FHA predicts larger capacitor voltage up to 100% larger.

The first row of Fig. 18 shows the normalized $I_{Lt_{v_A}\nearrow\text{-FHA}}$ predicted in (14) for $r = 1.1$, 1.3, and 1.5. The dashed lines separate CCM1 and CCM2 where $I_{Lt_{v_A}\nearrow\text{-FHA}}$ goes from positive to negative, generating ZVS. Knowing the largest $I_{Lt_{v_A}\nearrow\text{-FHA}}$ in CCM1 allows selecting the optimum value of auxiliary current to ensure soft switching for the entire operating points of the converter, for example, following the approach in [47]. Second row of Fig. 18 depicts the maximum $I_{Lt_{v_A}\nearrow}$ that is obtainable by inserting φ and M from (55) into (52). Comparing these figures show that the location of the maximum $I_{Lt_{v_A}\nearrow}$ is predicted differently in FHA and in time-domain methods. In addition, FHA predicts much larger $I_{Lt_{v_A}\nearrow}$ compared to the estimate of time-domain approach. Therefore, an auxiliary current designed based on FHA will inject unnecessarily large current to the ac node of the leading leg which incurs unwanted conduction losses.

VII. Experimental Results

Experimental verification of the merits of the proposed analytic predictions is provided in this section. The specifications of the prototype converter are given in Table III.

To consider the voltage drop of output diodes $V_{\text{out}} = V_{\text{out\_nom}} + 2 * 0.7 = 49.4$ V and $P = P_{\text{out\_nom}} * \frac{49.4}{48} = 103$ W. We select $n = 2$, $r = 1.1$, and $\varphi_{V_{\text{in\_min}}} = 150^\circ = \frac{5\pi}{6}$ rad. From (1)

$$M_{V_{\text{in\_min}}} = \frac{V_{\text{out}}}{V_{\text{in\_min}}/n} = \frac{49.4}{120/2} = 0.8233$$

$$M_{V_{\text{in\_max}}} = \frac{V_{\text{out}}}{V_{\text{in\_max}}/n} = \frac{49.4}{180/2} = 0.5489.$$

Inserting $\varphi_{V_{\text{in\_min}}}$, $M_{V_{\text{in\_min}}}$, and r in (69) gives $P_{\text{base\_}V_{\text{in\_min}}} = 131.35$ W. from (10), we find $Z_0 = 54.82\ \Omega$. Selecting $f_{\text{SW}} = 250$ kHz results in $\omega_0 = 1.4280$ Mrad/s and from (1) we reach to $L = 38.4\ \mu$H and $C = 12.8$ nF.

Due to loss of ZVS in CCM1, an adaptive auxiliary circuit is adopted as shown in Fig. 19 (introduced in [47]).

For $r = 1.1$, (56) gives $\varphi_{I_{Lt_{v_A}\nearrow\text{max}}} = 54^\circ$. Also, from Fig. 18, we have $I_{Lt_{v_A}\nearrow\text{max}} = 0.162\ I_{\text{base}}$. For $V_{\text{in}} = 180$ V from (7), we have $I_{\text{base}} = 5.16$ A which gives $I_{Lt_{v_A}\nearrow\text{max}} = 0.84$ A. The design formula for L_{aux} from [47] is

$$L_{\text{aux}} < \frac{TV_{\text{in}}}{16 I_{Lt_{v_A}\nearrow\text{max}}/n}\left(1 - \frac{1}{\pi}\varphi_{I_{Lt_{v_A}\nearrow\text{max}}}\right)$$

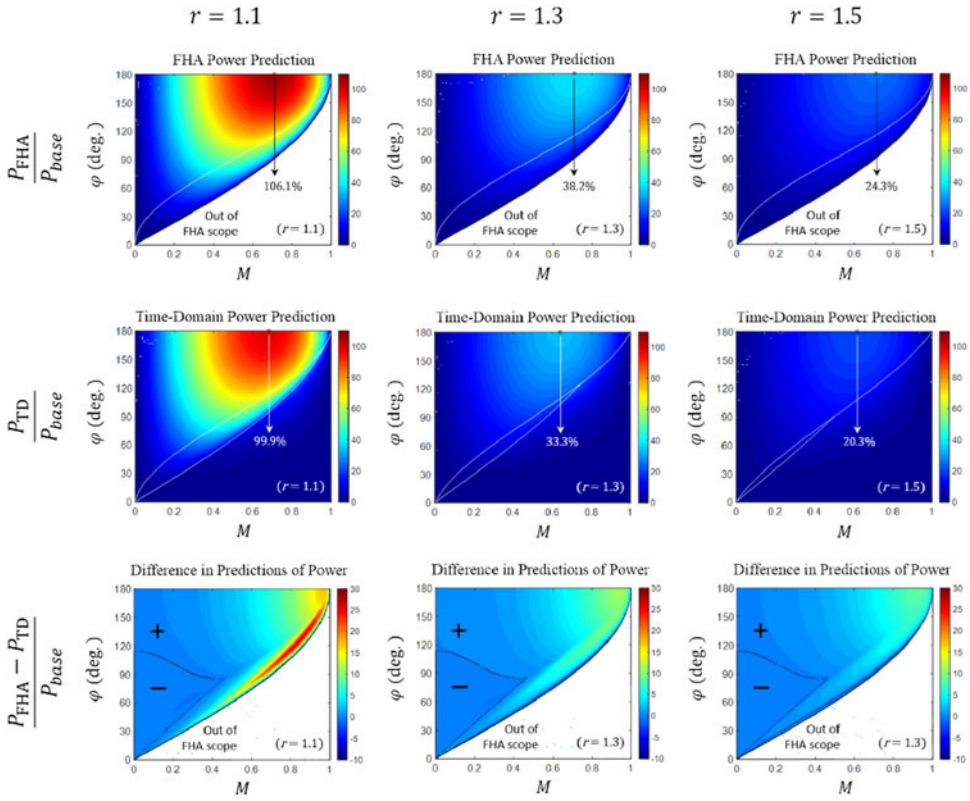

Fig. 14. Prediction of P/P_{base} percentage for $r = 1.1, 1.3$, and 1.5 bases on FHA (first row) and time-domain analysis (second row). White lines indicate mode boundaries. Difference in predictions is given in third row.

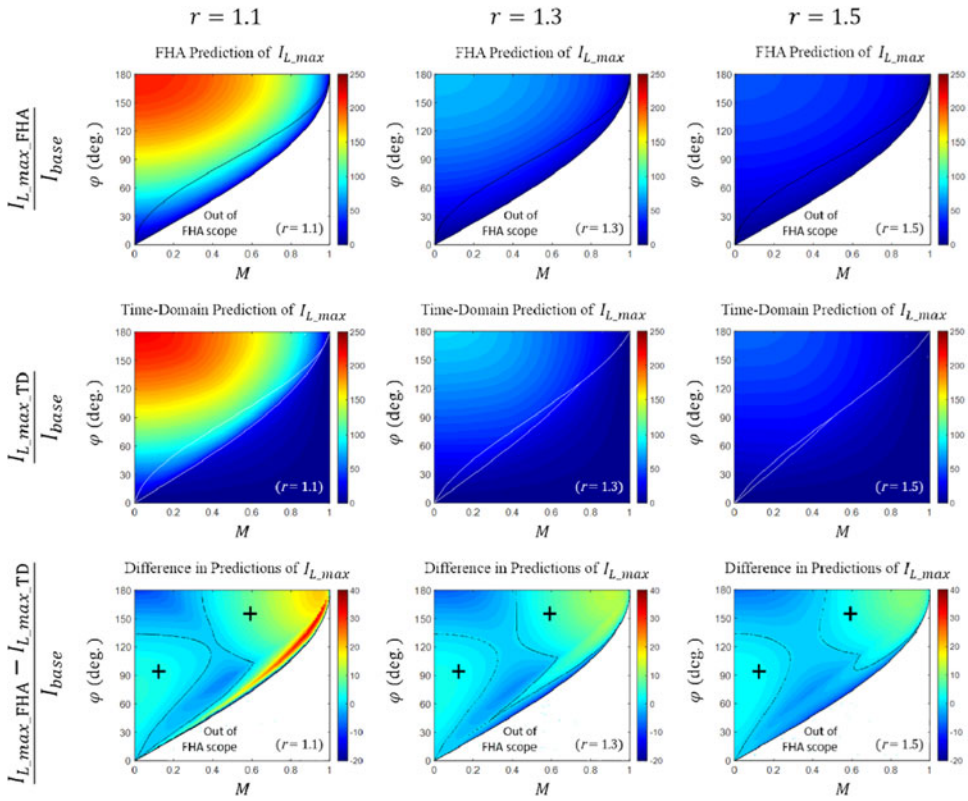

Fig. 15. Prediction of $I_{L\_\max}/I_{\mathrm{base}}$ percentage for $r = 1.1, 1.3$, and 1.5 bases on FHA (first row) and time-domain analysis (second row). Solid lines indicate mode boundaries. Difference in predictions is given in third row.

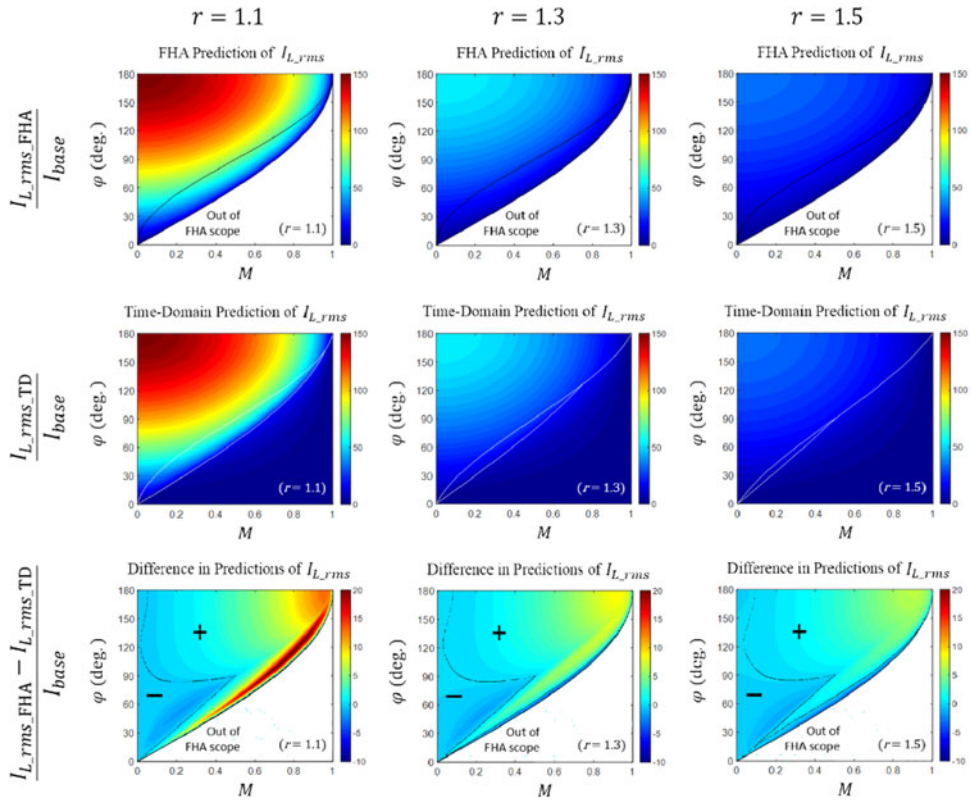

Fig. 16. Prediction of $I_{L\_\max}/I_{\text{base}}$ percentage for $r = \ 1.1, 1.3$, and 1.5 bases on FHA (first row) and time-domain analysis (second row). Solid lines indicate mode boundaries. Difference in predictions is given in third row.

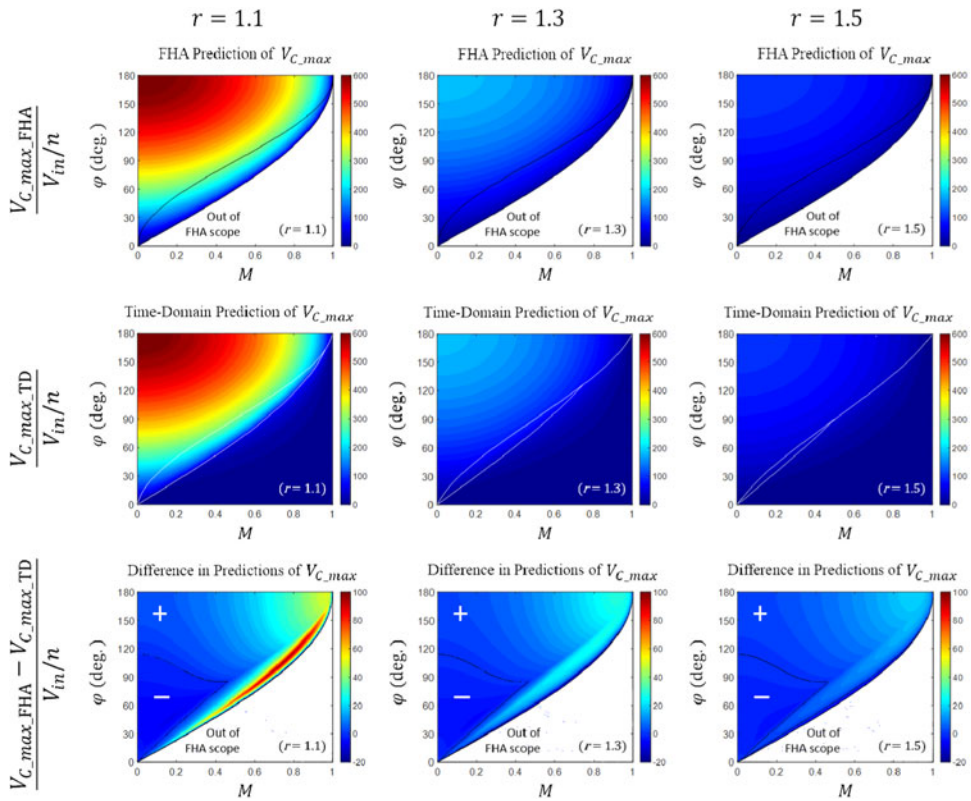

Fig. 17. Prediction of $V_{C\_\max}/(V_{\text{in}}/n)$ percentage r for $r = \ 1.1, 1.3$, and 1.5 bases on FHA (first row) and time-domain analysis (second row). Solid lines indicate mode boundaries. Difference in predictions is in third row.

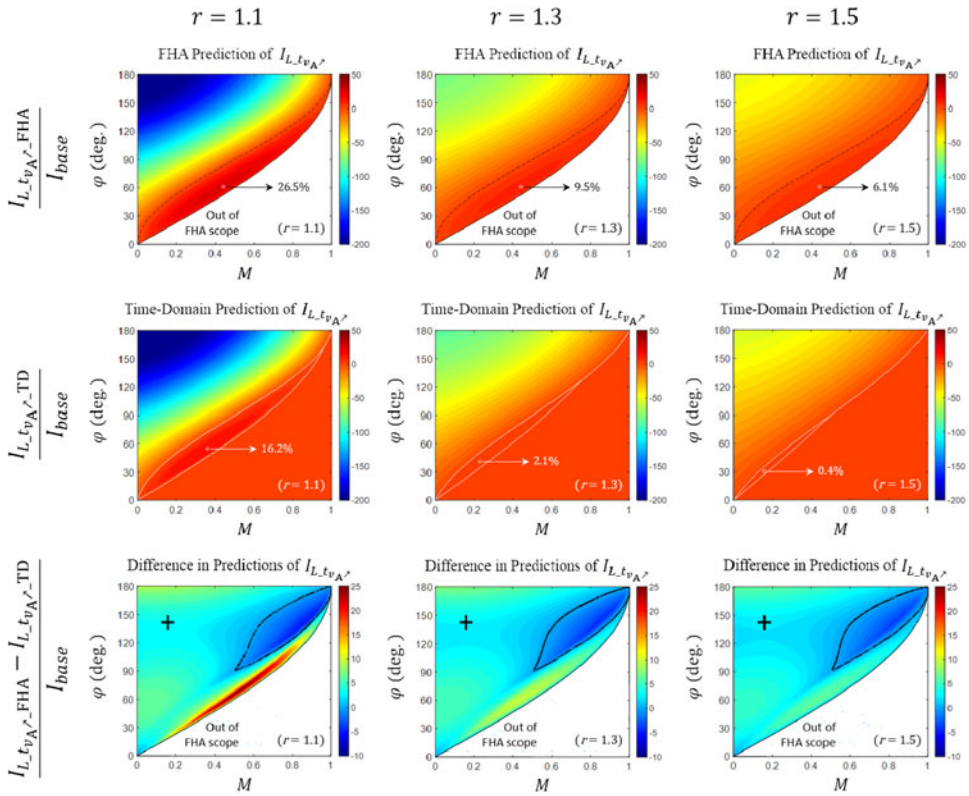

Fig. 18. Prediction of $I_{L+t_{v_{A'}}}/I_{\text{base}}$ percentage for $r = 1.1, 1.3$, and 1.5 bases on FHA (first row) and time-domain analysis (second row). Solid lines indicate mode boundaries. Difference in predictions is given in third row.

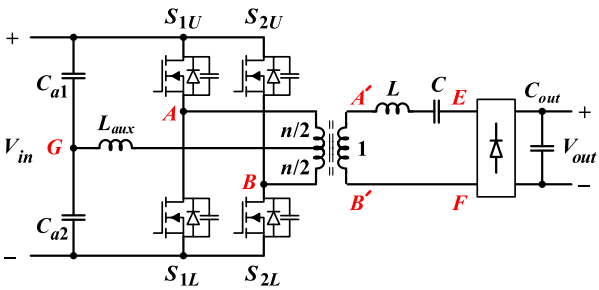

Fig. 19. SRC with full-bridge inverter and full-bridge diode rectifier.

TABLE III
PROTOTYPE CONVERTER SPECIFICATIONS

Symbol	Parameter	Value
$P_{\text{out\_nom}}$	Nominal output power	100 W
V_{in}	Input voltage	120–180 V
$V_{\text{out\_nom}}$	Nominal output voltage	48 V
f_{SW}	Switching frequency	≥200 kHz

which gives $L_{\text{aux}} < 75\ \mu$H. Table IV shows the real components of the converter.

The deadtime, denoted by t_d, was 100 ns and the switches were STW75NF30 with $R_{\text{ds}}(\text{on}) < 70\ \text{m}\Omega$ in warm state (110 °C junction temperature) and the effective drain–source capacitance of $C_{\text{sb}} = 2 \times 350$ nF. C_{sb} is the sum of charge equivalent (and not the energy equivalent) capacitors of S_{1L} and S_{1U} (calculated from [48, Fig. 9] using the method in [49, p. 247]) plus the stray capacitance of the transformer seen at the primary [50], [51]. Note that the value of 837 pF for C_{oss} mentioned in [48] should not be used for C_{sb} [49]. MOSFET drivers were FOD3180.

When measured, the physical capacitor chosen as the resonant capacitor showed an effective capacitance of 12.5 nF (which is within its tolerance range). Therefore, the selection of $f_{\text{SW}} = 250$ kHz means $r = 1.065$ and the tests are done using this r value.

Figs. 20 to 22 provide the experimental waveforms, the predictions of FHA and time-domain methods and the measured experimental values for operation in DCM, CCM1, and CCM2, respectively. In each mode, there are two tests for V_{in} of 120 and 180 V, respectively. For the majority of the tests, the output voltage was kept constant at the desired 49.4 V using an electronic load model Sorensen slm 60v/15a/75w in constant voltage mode.

Fig. 20 shows the main waveforms for DCM mode. FHA has no prediction for this mode. For both tests for V_{in} equal to 120 and 180 V, there is a close agreement between the experimental results of all the variables with the analytical predictions from the time-domain method. The readers can refer to the accompanied "SRC_Modes" calculator described in the Appendix.

Fig. 21 represents the experimental outcomes in CCM1 mode when the auxiliary circuit is disconnected. The time-domain predictions are closer to the measurements than FHA predictions.

TABLE IV
PROTOTYPE CONVERTER COMPONENTS

Component	Value
Switches	STW75NF30
Drivers	FOD3180
Main transformer	ETD39, 3F3, 2:1 Leakage Inductance (Primary) $<$400 nH Magnetizing inductance (primary) $>$ 5 mH
Resonant inductor	RM10, 3F3, 19t, gap: 1 mm, 37 μH
Resonant capacitor	Film MMKP 13 nF, 1600 Vdc
Rectifier diodes	PDS5100
Output capacitor	250 μF, 100 V
Auxiliary inductors	RM10, 3F3, 19t, gap: 0.5 mm, 70 μH
Auxiliary capacitors	100 μF, 100 V

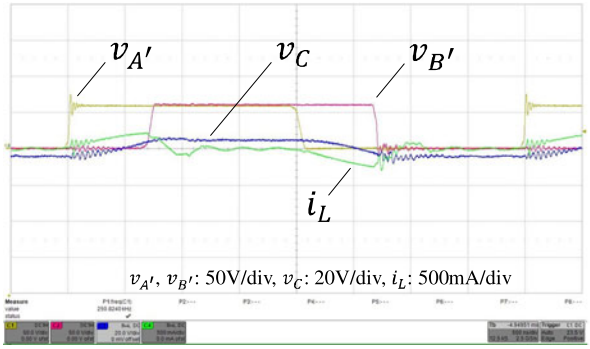

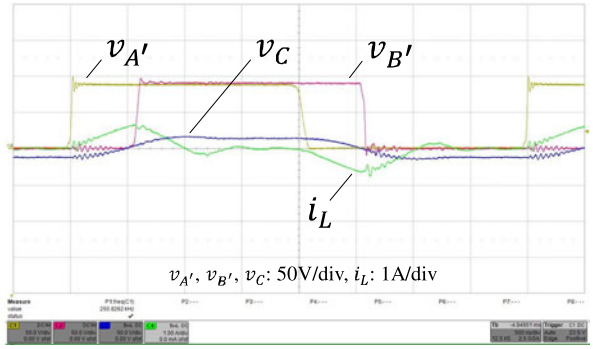

	Exp.	TD	FHA
V_{in} (V)	120		
V_{out} (V)	49.4		
M	0.8234		
φ (deg.)	80	80	--
Mode	DCM	DCM	--
P (W)	4.2	5.4	--
I_{L_max} (A)	0.30	0.34	--
I_{L_rms} (A)	0.13	0.17	--
V_{C_max} (V)	6.5	8.8	--
$I_{L\_t_{v_A\nearrow}}$ (A)	0.0	0.0	--

	Exp.	TD	FHA
V_{in} (V)	180		
V_{out} (V)	49.4		
M	0.5490		
φ (deg.)	80	80	--
Mode	DCM	DCM	--
P (W)	11.5	13.2	--
I_{L_max} (A)	0.62	0.89	--
I_{L_rms} (A)	0.33	0.40	--
V_{C_max} (V)	16.6	21.4	--
$I_{L\_t_{v_A\nearrow}}$ (A)	0.0	0.0	--

Fig. 20. Experimental results in DCM mode at $V_{\rm in}$ of 120 V (left) and of 180 V (right). $(r = 1.065)$.

An important observation that in CCM1 the time-domain analysis slightly underestimates the values of $I_{L\_t_{v_A\nearrow}}$ while FHA overestimates. The voltage spikes in $v_{A'}$ are the indication of loss of ZVS without the auxiliary circuit connected. To get the ZVS, the value of $L_{\rm aux}$ was reduced from 70 to 51 μH (to account for the underestimation).

Fig. 22 shows the experimental outcomes in CCM1 mode. For the test at $V_{\rm in} = 120$ V, we have $V_{\rm out} = 49.4$ V; however, in the case of $V_{\rm in} = 180$ V, it was not possible to keep $V_{\rm out}$ at 49.4 V due to the restrictions of the available electronic load. Therefore, the test at $V_{\rm in} = 180$ V was performed using a resistive load which resulted in $V_{\rm out} = 85.5$ V. Again the time-domain approach predictions are closer to the measurement values compared with the FHA predictions. Similar to the case of CCM1, the time-domain analysis predicts less negative values for $I_{L\_t_{v_A\nearrow}}$ compared with the measurement results. This is also true for FHA in this mode. The reason for this difference is believed to originate from the nonzero deadtime in the experimental setup.

VIII. EFFECT OF NONZERO DRAIN–SOURCE CAPACITANCE AND DEADTIME

Previously, it was mentioned that a negative $I_{L\_t_{v_A\nearrow}}$ is required at $t_{v_A\nearrow}$ in order to have ZVS in the leading leg because $I_{L\_t_{v_A\nearrow}} < 0$ provides the energy needed for changing/discharging the drain–source capacitors of the switches. This means that $I_{L\_t_{v_A\nearrow}}$ should charge a total effective capacitor denoted by $C_{\rm sb}$ from 0 to $V_{\rm in}$. Having a nonzero t_d, we can assume that $I_{L\_t_{v_A\nearrow}}$ remains essentially constant during t_d; therefore, the condition for a full ZVS (i.e., during t_d) is

$$I_{L\_t_{v_A\nearrow}} < -C_{\rm sb} V_{\rm in}/t_d. \tag{83}$$

The rationale behind this assumption is that the stored energy in the resonant tank ensures the current flow during t_d provided that $t_d < T/20$. Table V shows the different possibilities for leading leg switching and their conditions. The case of "reduced turn-ON switching losses" comes from the fact that if $I_{L\_t_{v_A\nearrow}}$ is not sufficiently negative, the voltage of $C_{\rm sb}$ cannot change from

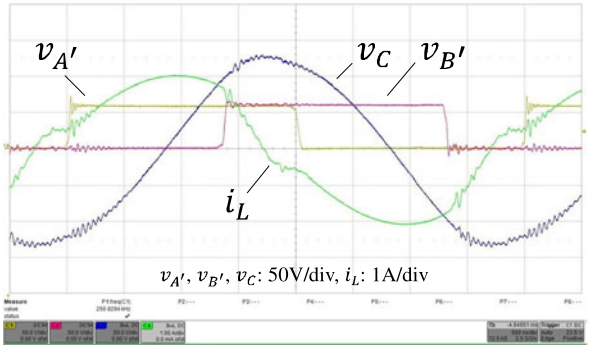

	Exp.	TD	FHA
V_{in} (V)	120		
V_{out} (V)	49.4		
M	0.8234		
φ (deg.)	121	121	121
Mode	CCM1	CCM1	CCM1
P (W)	68.5	65.2	98.80
$I_{L\_\max}$ (A)	2.15	2.11	3.14
$I_{L\ rms}$ (A)	1.63	1.49	2.22
V_{C_max} (V)	124.0	105.8	160.5
$I_{L\_t_{v_{A'}}}$ (A)	+0.45	+0.29	+0.58

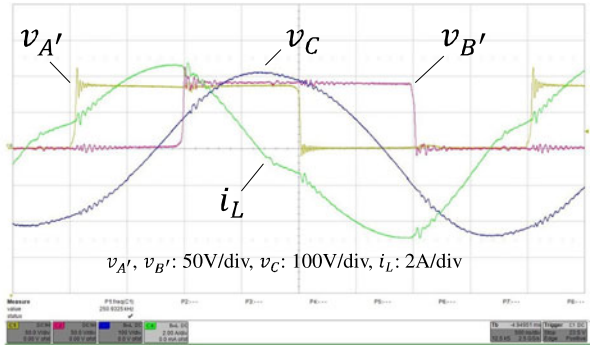

	Exp.	TD	FHA
V_{in} (V)	180		
V_{out} (V)	49.4		
M	0.5490		
φ (deg.)	78	78	78
Mode	CCM1	CCM1	CCM1
P (W)	141.4	138.4	161.8
$I_{L\_\max}$ (A)	4.80	4.78	5.14
$I_{L\ rms}$ (A)	3.22	3.18	3.64
V_{C_max} (V)	236.0	224.8	262.6
$I_{L\_t_{v_{A'}}}$ (A)	+1.65	+1.32	+1.9

Fig. 21. Experimental results in CCM1 mode at $V_{\rm in}$ of 120 V (left) and of 180 V (right). $(r = 1.065)$.

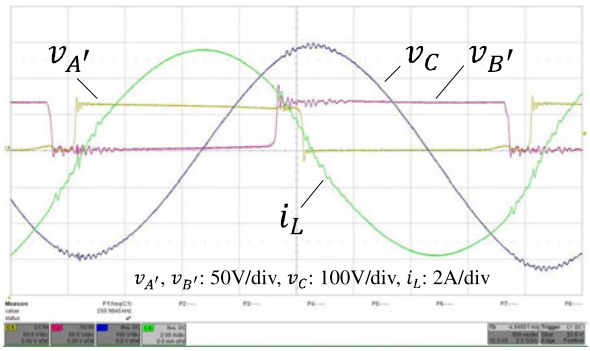

	Exp.	TD	FHA
V_{in} (V)	120		
V_{out} (V)	49.4		
M	0.8234		
φ (deg.)	180	180	180
Mode	CCM2	CCM2	CCM2
P (W)	182.4	181.9	196.5
$I_{L\_\max}$ (A)	5.72	5.63	6.25
$I_{L\ rms}$ (A)	4.13	4.06	4.42
V_{C_max} (V)	298.0	295.4	319.1
$I_{L\_t_{v_{A'}}}$ (A)	-1.90	-3.08	-3.05

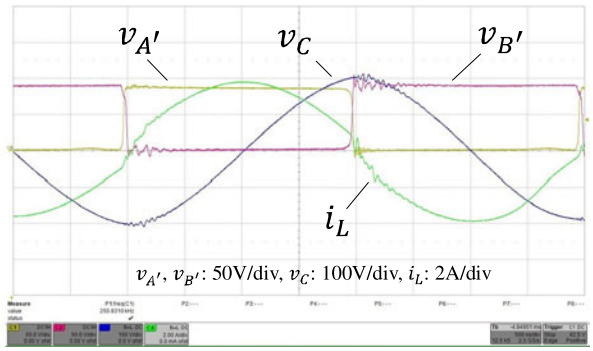

	Exp.	TD	FHA
V_{in} (V)	180		
V_{out} (V)	85.5		
M	0.95		
φ (deg.)	180	180	180
Mode	CCM2	CCM2	CCM2
P (W)	244.0	229.9	284.0
$I_{L\_\max}$ (A)	4.25	4.01	5.22
$I_{L\ rms}$ (A)	3.16	2.94	3.69
V_{C_max} (V)	225.1	215.8	266.6
$I_{L\_t_{v_{A'}}}$ (A)	-1.25	-1.67	-1.63

Fig. 22. Experimental results in CCM2 mode at $V_{\rm in}$ of 120 V (left) and of 180 V (right). $(r = 1.065)$. To keep the current levels within the range, the test for $V_{\rm in} = 180$ V is performed at $V_{\rm out} = 85.5$ V.

0 to $V_{\rm in}$ during t_d (or during t_d). This case would not happen if $C_{\rm sb} = 0$.

The consequence of having a nonzero $C_{\rm sb}$ is that now the entire region of CCM2 does not have full ZVS, but it is divided to two distinct regions with "reduced turn-ON switching losses" and with ZVS. Fig. 23 depicts the actual (not normalized) $I_{L\_t_{v_{A'}}}$ values for our system with $L = 13$ μH, $C = 12.5$ nF, $V_{\rm in} = 120$ V, $t_d = 100$ ns, $C_{\rm sb} = 2 \times 350$ nF, and $r = 1.1$, 1.3, and 1.5. The current threshold of $-C_{\rm sb}V_{\rm in}/t_d = -0.84$ A is shown and the split of CCM2 region to two distinct regions is illustrated. In addition, although we know from [49] that $C_{\rm sb}$ is voltage dependent, its values does not change much from $V_{\rm in} = 120$ to 180 V; therefore, Fig. 23 is not repeated for $V_{\rm in} = 180$ V.

TABLE V
LEADING LEG TURN-ON SWITCHING POSSIBILITIES AND THEIR CONDITIONS FOR FINITE DEADTIME

Possibility	Condition	Comment
No soft switching	$I_{L\_t_{v_{\mathrm{A}}\nearrow}} > 0$	Hard switching at $t_{v_{\mathrm{A}}\nearrow}$
Zero current switching	$I_{L\_t_{v_{\mathrm{A}}\nearrow}} = 0$	
Reduced turn-on switching losses	$0 > I_{L\_t_{v_{\mathrm{A}}\nearrow}} > -C_{\mathrm{sb}} V_{\mathrm{in}}/t_d$	$\Delta V_{C_{\mathrm{sb}}} < V_{\mathrm{in}}$ during t_d
ZVS	$-C_{\mathrm{sb}} V_{\mathrm{in}}/t_d > I_{L\_t_{v_{\mathrm{A}}\nearrow}}$	$\Delta V_{C_{\mathrm{sb}}} = V_{\mathrm{in}}$ during t_d

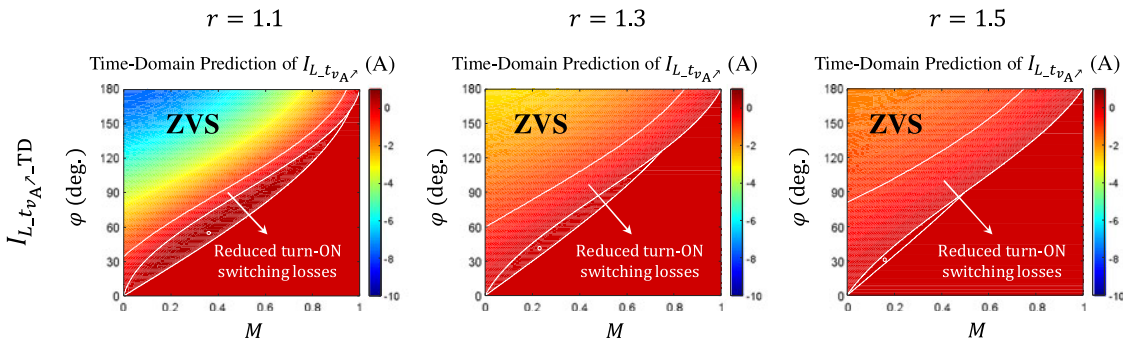

Fig. 23. Time-domain prediction of $I_{L\_t_{v_{\mathrm{A}}\nearrow}}$ for $V_{\mathrm{in}} = 120\,\mathrm{V}, t_d = 100\,\mathrm{ns}, C_{\mathrm{sb}} = 2 \times 350\,\mathrm{pF}$ and $r = 1.1,\ 1.3\ 1.1,\ 1.3$, and 1.5. CCM2 is divided to two regions with "reduced turn-ON switching losses" and ZVS, separated at $-0.84\,\mathrm{A}$.

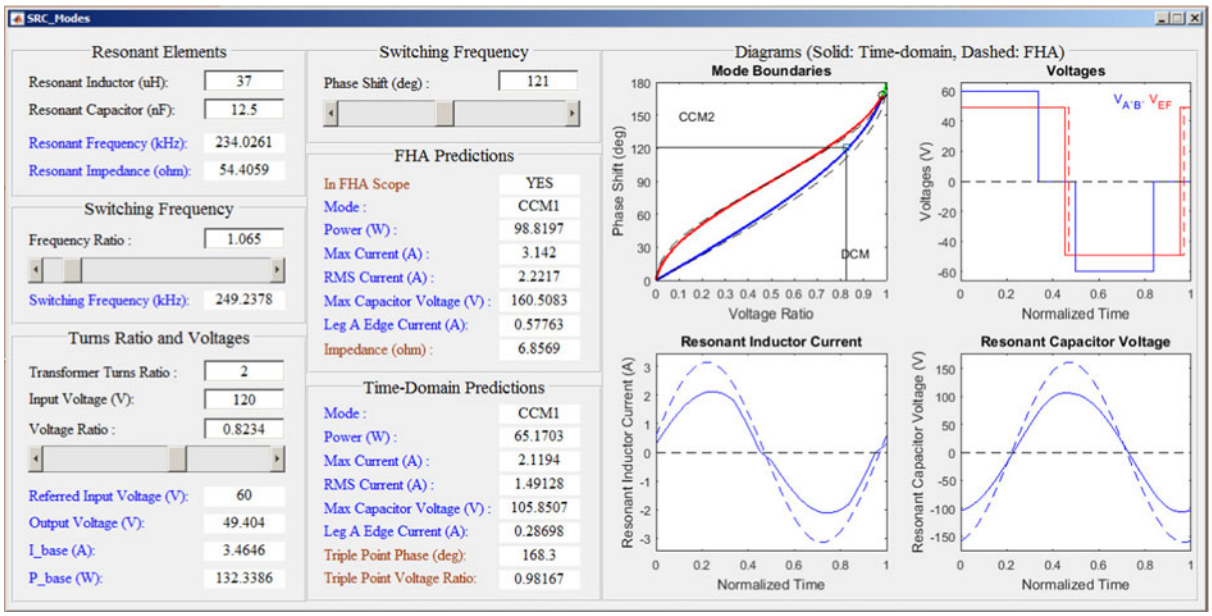

Fig. 24. SRC_Modes Panel.

It is important to note that everywhere in this paper the value of φ is defined based on the power waveforms and not based on the gate signals. The reason is that with a nonzero deadtime, the time-wise compatibility between the power waveforms and gate signals exists only when ZVS is maintained. When the circuit operates without a full ZVS in the leading leg, there is a mismatch between the gate signals and power waveforms as large as the deadtime. This phenomenon is reported in [52] and [53] for a different type of converter. Defining φ based on the power waveforms eliminates the dependence of phase shift on the soft-switching condition.

IX. CONCLUSION

A comprehensive time-domain analysis of phase-shift-modulated SRCs operating above resonance is presented. Closed-form formulas are derived using two methods of FHA technique and the proposed time-domain analysis. Three

mutually exclusive and collectively exhaustive modes of operation are identified. The accuracy of the first harmonic approximation is examined and closed-form equations for the boundary conditions of the three operation modes are provided. An adaptive passive auxiliary circuit to guarantee ZVS for the entire operating conditions is suggested. The predictions of both analytical methods were examined by comparing to experimental results from a 100 W prototype.

APPENDIX

This paper has an active content program, named as "SRC_Modes" calculator to calculate and visualize the modes, represent the waveforms and deliver the main quantities using both FHA and time-domain approaches, as shown in Fig. 24. The user selects values for L, C, n, $V_{\rm in}$, r, M and φ where there are individual sliders for r, M, and φ.

Note that all three files of the "SRC_Modes" calculator must be in the same folder in order to run correctly. The file names are:

1) *SRC_Modes.m*, the main m file to run;
2) *SRC_Modes.fig*, the fig file including the visual panel; and
3) *Calc1.m*, the function file including the calculations.

REFERENCES

[1] F. C. Schwarz, "An improved method of resonant current pulse modulation for power converters," in *Proc. Power Electron. Spec. Conf.*, Culver City, CA, USA, 1975, pp. 194–204.

[2] A. Emadi, S. S. Williamson, and A. Khaligh, "Power electronics intensive solutions for advanced electric, hybrid electric, and fuel cell vehicular power systems," *IEEE Trans. Power Electron.*, vol. 21, no. 3, pp. 567–577, May 2006.

[3] P. A. Cassani and S. S. Williamson, "Design, testing, and validation of a simplified control scheme for a novel plug-in hybrid electric vehicle battery cell equalizer," *IEEE Trans. Ind. Electron.*, vol. 57, no. 12, pp. 3956–3962, Dec. 2010.

[4] H. Wang and A. Khaligh, "Comprehensive topological analyses of isolated resonant converters in PEV battery charging applications," in *Proc. Transp. Electrif. Conf. Expo*, Detroit, Michigan, USA, 2013, pp. 1–7.

[5] P. Ranstad, H.-P. Nee, J. Linner, and D. Peftitsis, "An experimental evaluation of SiC switches in soft-switching converters," *IEEE Trans. Power Electron.*, vol. 29, no. 3, pp. 2527–2583, May 2014.

[6] E. Stenglein, C. Oeder, and T. Duerbaum, "Design of a series resonant converter with inductive output filter for 130 W street lighting application," in *Proc. Int. Exhib. Conf. Power Electron. Intell. Motion Renewable Energy Energy Manage.*, Nuremberg, Germany, 2015, pp. 1–7.

[7] M. Momeni, H. Meshgin Kelk, and H. Talebi, "Rotating switching surface control of series-resonant converter based on a piecewise affine model," *IEEE Trans. Power Electron.*, vol. 30, no. 3, pp. 1762–1772, Mar. 2015.

[8] A. Knott, T. M. Andersen, P. Kamby, J. A. Pedersen, M. P. Madsen, M. Kovacevic, and M. A. E. Andersen, "Evolution of very high frequency power supplies," *IEEE J. Emerg. Sel. Top. Power Electron.*, vol. 2, no. 3, pp. 386–394, Sep. 2014.

[9] A. Safaee, A. Bakhshai, and P. Jain, "An efficient adaptive energy storage using saturable inductors for ZVS phase-shift-modulated full-bridge converters," in *Proc. Int. Conf. Power Control Embedded Syst.*, Allahabad, India, 2010, pp. 1–5.

[10] S.-H. Lee, Y.-W. Cho, W.-J. Cha, K.-T. Kim, and B.-H. Kwon, "High efficient series resonant converter using direct power conversion," *IET Power Electron.*, vol. 7, no. 12, pp. 3045–3051, Dec. 2014.

[11] B. Yang, S. Du, W. Chen, C. Deng, and D. Xu, "Optimal parameters design for series-series resonant converter for wireless power transfer," in *Proc. Int. Power Electron. Appl. Conf. Expo.*, Shanghai, China, 2014, pp. 772–777.

[12] N. Bailian, C. Y. Chung, and H. L. Chan, "Design and comparison of parallel and series resonant topology in wireless power transfer," in *Proc. IEEE 8th Conf. Ind. Electron. Appl.*, Melbourne, Australia, 2013, pp. 1832–1837.

[13] F. Musavi, M. Edington, and W. Eberle, "Wireless power transfer: A survey of EV battery charging technologies," in *Proc. IEEE Energy Convers. Congr. Expo.*, Raleigh, NC, USA, 2012, pp. 1804–1810.

[14] G. Moschopoulos and P. Jain, "A series-resonant DC/DC converter with asymmetrical PWM and synchronous rectification," in *Proc. Power Electron. Spec. Conf.*, Galway, Ireland, 2000, vol. 3, pp. 1522–1527.

[15] S. Chopra and P. Bauer, "Analysis and design considerations for a contactless power transfer system," in *Proc. IEEE 33rd Int. Telecommun. Energy Conf.*, Amsterdam, The Netherlands, 2011, pp. 1–6.

[16] M. A. Bloom, N. Geng, and M. Krishnamurthy, "Design considerations for wireless electric vehicle charging," in *Proc. Transp. Electrif. Conf. Expo*, Detroit, MI, USA, 2013, pp. 1–6.

[17] M. K. Kazimierczuk and S. Wang, "Frequency-domain analysis of series resonant converter for continuous conduction mode," *IEEE Trans. Power Electron.*, vol. 7, no. 2, pp. 270–279, Apr. 1992.

[18] V. Vorperian and S. Cuk, "A complete DC analysis of the series resonant converter," in *Proc. Power Electron. Spec. Conf.*, Cambridge, MA, USA, 1982, pp. 85–100.

[19] R. L. Steigerwald, "A comparison of half-bridge resonant converter topologies," *IEEE Trans. Power Electron.*, vol. 3, no. 2, pp. 174–182, Apr. 1988.

[20] P. Jain, "A novel frequency domain modelling of a series resonant DC/DC converter," in *Proc. Int. Telecommun. Energy Conf.*, Orlando, FL, USA, 1990, pp. 343–350.

[21] C. Q. Lee and K. Siri, "Analysis and design of series resonant converter by state-plane diagram," *IEEE Trans. Aerosp. Electron. Syst.*, vol. AES-22, no. 6, pp. 757–763, Nov. 1986.

[22] H. A. Kojori, S. B. Dewan, and J. D. Lavers, "Steady-state analysis and design optimization of an inductor-transformer resonant DC-DC converter," *IEEE Trans. Ind. Appl.*, vol. 27, no. 3, pp. 515–522, May/Jun. 1991.

[23] F.-S. Tsai and F. C. Lee, "A complete DC characterization of a constant-frequency, clamped-mode, series-resonant converter," in *Proc. Power Electron. Spec. Conf.*, Kyoto, Japan, 1988, pp. 987–996.

[24] F.-S. Tsai, P. Materu, and F. C. Lee, "Constant-frequency clamped-mode resonant converters," *IEEE Trans. Power Electron.*, vol. 3, no. 4, pp. 460–473, Oct. 1988.

[25] A. F. Wittulski and R. W. Erickson, "Steady-state analysis of the series resonant," *IEEE Trans. Aerosp. Electron. Syst.*, vol. AES-21, no. 6, pp. 791–799, Nov. 1985.

[26] R. King and T. A. Stuart, "A normalized model for the half-bridge series resonant converter," *IEEE Trans. Aerosp. Electron. Syst.*, vol. AES-17, no. 2, pp. 190–198, Mar. 1981.

[27] R. Oruganti and F. C. lee, "Resonant power processors, Part I—State plane analysis," *IEEE Trans. Ind. Appl.*, vol. IA-21, no. 6, pp. 1453–1460, Nov. 1985.

[28] A. S. Kislovski, "A contribution to steady-state modeling of half-bridge series-resonant power cells," *IEEE Trans. Power Electron.*, vol. PE-1, no. 3, pp. 161–166, Jul. 1986.

[29] L. Fiorella, C. Di Miceli, T. Raimondi, and C. Cutrona, "Analysis of a series resonant converter," in *Proc. Int. Telecommun. Energy Conf.*, Florence, Italy, 1989, vol. 2, pp. 20.3/1–20.3/6.

[30] A. K. S. Bhat, "A generalized steady-state analysis of resonant converters using two-port model and Fourier-series approach," *IEEE Trans. Power Electron.*, vol. 13, no. 1, pp. 142–151, Jan. 1998.

[31] T. H. Sloane, "Design of high-efficiency series-resonant converters above resonance," *IEEE Trans. Aerosp. Electron. Syst.*, vol. 62, no. 2, pp. 393–402, Mar. 1990.

[32] B. Lee and H. Cha, "Comparative analysis of charging modes of series-resonant converter for an energy storage capacitor," *IEEE Trans. Plasma Sci.*, vol. 41, no. 3, pp. 570–577, Mar. 2013.

[33] H.-J. Jiang, G. Maggetto, and P. Lataire, "Steady-state analysis of the series resonant DC-DC converter in conjunction with loosely-coupled transformer-above resonance operation," *IEEE Trans. Power Electron.*, vol. 14, no. 3, pp. 469–480, May 1999.

[34] R. J. King and T. A. Stuart, "A large-signal dynamic simulation for the series resonant converter," *IEEE Trans. Aerosp. Electron. Syst.*, vol. AES-19, no. 6, pp. 859–870, Nov. 1983.

[35] E. X. Yang, F. C. Lee, and M. M. Jovanovic, "Small-signal modeling of series and parallel resonant converters," in *Proc. Appl. Power Electron. Conf.*, Boston, MA, USA, 1992, pp. 785–792.

[36] A. M. Stankovic, D. J. Perreault, and K. Sato, "Synthesis of dissipative nonlinear controllers for series resonant DC/DC converters," *IEEE Trans. Power Electron.*, vol. 14, no. 4, pp. 673–682, Jul. 1999.

[37] K. D. T. Ngo, "Analysis of a series resonant converter pulse width-modulated or current-controlled for low switching loss," *IEEE Trans. Power Electron.*, vol. 3, no. 1, pp. 55–63, Jan. 1988.
[38] J. M. Burdio, F. Canales, P. M. Barbosa, and F. C. Lee, "Comparison study of fixed-frequency control strategies for ZVS DC/DC series resonant converters," in *Proc. Power Electron. Spec. Conf.*, Vancouver, BC, Canada, 2001, vol. 1, pp. 427–432.
[39] J. P. Vandelac and P. D. Ziogas, "A DC to DC PWM series resonant converter operated at resonant frequency," *IEEE Trans. Power Electron.*, vol. 35, no. 3, pp. 451–460, Aug. 1988.
[40] J. Sabaté and F. C. Lee, "Offline application of the fixed-frequency clamped-mode series resonant converter," *IEEE Trans. Power Electron.*, vol. 6, no. 1, pp. 39–47, Jan. 1991.
[41] B. S. Nathan and V. Ramanarayanan, "Analysis, simulation and design of series resonant converter for high voltage applications," in *Proc. IEEE Int. Conf. Ind. Technol.*, Goa, India, 2000, pp. 688–693.
[42] J. S. Glaser, A. F. Witulski and R. G. Myers, "Steady-state analysis of the constant-frequency clamped series resonant converter," *IEEE Trans. Aerosp. Electron. Syst.*, vol. 30, no. 1, pp. 135–143, Jan. 1994.
[43] A. A. Aboushady, K. H. Ahmed, S. J. Finney, and B. W. Williams, "Steady-state analysis of full-bridge series resonant converter with phase-shift and frequency control," in *Proc. 5th IET Int. Conf. Power Electron. Mach. Drives*, Brighton, U.K., 2010, pp. 1–6.
[44] Y. V. Singh, K. Viswanathan, R. Naik, J. A. Sabate, and R. Lai, "Analysis and control of phase-shifted series resonant converter operating in discontinuous mode," in *Proc. Appl. Power Electron. Conf.*, Long Beach, CA, USA, 2013, pp. 2092–2097.
[45] A. Safaee, P. Jain, and A. Bakhshai, "Time-domain steady-state analysis of fixed-frequency series resonant converters with phase-shift modulation," in *Proc. Transp. Electrif. Conf. Expo*, Detroit, MI, USA, 2014, pp. 1–7.
[46] F. M. Ibanez, J. Vadillo, J. M. Echeverria, and L. Fontan, "Anomalous step-up behavior in discontinuous series resonant converters," in *Proc. 15th Workshop Control Model. Power Electron.*, Santander, Spain, 2014, pp. 1–6.
[47] A. Safaee, K. Woronowicz, P. Jain, and A. Bakhshai, "A robust fixed-frequency soft switching series resonant converter for transportation applications," in *Proc. IEEE Int. Electr. Vehicle Conf.*, Florence, Italy, 2014, pp. 1–6.
[48] [Online], 2008 Available: http://www.st.com/content/ccc/resource/technical/document/datasheet/83/05/21/55/4b/b3/44/12/CD00174580.pdf/files/CD00174580.pdf/jcr:content/translations/en.CD00174580.pdf
[49] F. Krismer, "Modeling and optimization of bidirectional dual active bridge DC–DC converter topologies," Ph.D. dissertation, Dept. Elect. Eng., ETH Zurich, Switzerland, 2010.
[50] A. Safaee, P. Jain, and A. Bakhshai, "A ZVS pulse width modulation full bridge converter with a low-RMS-current resonant auxiliary circuit," *IEEE Trans. Power Electron.*, vol. 31, no. 6, pp. 4031–4047, Jun. 2016.
[51] A. Safaee, P. Jain, and A. Bakhshai, "An adaptive ZVS full-bridge DC–DC converter with reduced conduction losses and frequency variation range," *IEEE Trans. Power Electron.*, vol. 30, no. 8, pp. 4107–4118, Aug. 2015.
[52] D. Segaran, B. P. McGrath, and D. G. Holmes, "Adaptive dynamic control of a bi-directional DC-DC converter," in *Proc. IEEE Energy Convers. Congr. Expo.*, Atlanta, GA, USA, 2010, pp. 1442–1449.
[53] D. Segaran, D. G. Holmes, and B. P. McGrath, "Enhanced load step response for a bi-directional DC-DC converter," in *Proc. IEEE Energy Convers. Congr. Expo.*, Phoenix, AZ, USA, 2011, pp. 3649–3656.

Alireza Safaee (S'08–M'12–SM'14) received the B.Sc. degree in electrical engineering from the Isfahan University of Technology, Isfahan, Iran, the M.Sc. degree in physics from the Sharif University of Technology, Tehran, Iran, the Ph.D. degree in engineering from the University of Quebec, Chicoutimi, QC, Canada, and the second Ph.D. degree in power electronics from Queen's University, Kingston, ON, Canada, in 1997, 1999, 2009, and 2015, respectively.

From 1997 to 2005, he was a Design Engineer and later a Design Manager at Manabe Taghzyeh Electronic Company, Tehran, Iran, where his teams developed several types of chargers, inverters, stabilizers, and UPS systems for more than 1000 communication sites and power plants. From 2011 to June 2014, he was an Electrical Analyst at Bombardier Transportation. He is currently a Principal Power Electronics Engineer at OSRAM Sylvania, Danvers, MA, USA. His research interests include power electronics, magnetic design, resonant and soft-switching converters, and their control methods toward applications in aviation and renewable energy systems.

Masoud Karimi-Ghartemani (M'01–SM'09) received the Ph.D. degree in electrical engineering from the University of Toronto, Toronto, ON, Canada, in 2004.

He was an Assistant Professor at the Sharif University of Technology, Tehran, Iran, from 2005 to 2008. He was with the Queens Centre for Energy and Power Electronics Research, Queens University, Kingston, Canada, from 2008 to 2011. He is currently an Associate Professor in the Department of Electrical and Computer Engineering, Mississippi State University, Starkville, MS, USA. His research interests include control of distributed and renewable energy resources, microgrid, power system stability and control, power system measurement, and power quality.

Praveen K. Jain (S'86–M'88–SM'91–F'02) received the B.E. degree (Hons.) from the University of Allahabad, Allahabad, India, and the M.A.Sc. and Ph.D. degrees from the University of Toronto, Toronto, ON, Canada, in 1980, 1984, and 1987, respectively, all in electrical engineering.

He is currently a Professor of electrical and computer engineering at Queen's University, Kingston, ON, Canada, Tier 1 Canada Research Chair in power electronics, and the Director of the Queen's Centre for Energy and Power Electronics Research. He made pioneering contributions in introducing resonant power conversion technology in telecommunications during his work at Nortel in the 1990's. He played a key role in the design and development of high frequency power conversion equipment for the International Space Station at Canadian Astronautics in the late 1980s. Over the last 30 years, he has made sustained contributions to the theory and practice of power electronics through his considerable work with industry, including Astec, Freescale, General Electric, Intel and Nortel. He is the founder of two successful start-up companies, CHiL Semiconductor in the area of digital power controller (acquired by International Rectifier), and SPARQ Systems in the area of photovoltaic microinverters. He has supervised and guided more than 85 graduate students, postdoctoral fellows, and power electronics engineers who are well placed in industry and academia. He has published more than 450 papers and holds 50 patents.

Dr. Jain has received many awards and honors which include: Queen's Prize for Excellence in Research, IEEE William Newell Power Electronics Award, IEEE IAS Distinguished Lecturer, Fellow of the Royal Society of Canada, Fellow of the Engineering Institute of Canada, Fellow of the Canadian Academy of Engineering, and Engineering Medal of the Professional Engineers of Ontario.

Alireza Bakhshai (M'04–SM'09) received the B.Sc. and M.Sc. degrees from the Isfahan University of Technology, Isfahan, Iran, in 1984 and 1986, respectively, and the Ph.D. degree from Concordia University, Montreal, QC, Canada, in 1977.

From 1986 to 1993 and from 1998 to 2004, he was in the faculty of the Department of Electrical and Computer Engineering, Isfahan University of Technology. From 1997 to 1998, he was a Postdoctoral Fellow with Concordia University. He is currently with the Department of Electrical and Computer Engineering, Queen's University, Kingston, ON, Canada. His research interests include high-power electronics and applications in distributed generation and wind energy, control systems, and flexible ac transmission services.